Francisco Maria Cristão Marques Luquet Brasil

Bachelor of Science in Physics Engineering

Size-selected silver clusters on polymer surfaces as plasmonic transducers for nano-biosensors

Dissertation to obtain the Master degree in

Physics Engineering

Supervisor: Prof. Dr. Ana Gomes Silva, FCT-UNL

Jury:

President: Doctor Maria Isabel Simões Catarino

Arguer: Doctor Pedro Viana Baptista

Vowel: Doctor Ana Cristina Gomes da Silva

FACULDADE DE CIÊNCIAS E TECNOLOGIA
UNIVERSIDADE NOVA DE LISBOA

May 2017

"Size-selected silver clusters on polymer surfaces as plasmonic transducers for nano-bio sensors."

"I don't know where I'm going from here,

but I promise it won't be boring.

- David Bowie

Acknowledgments

First and foremost, I would like to thank Professor Dr. Vladimir Popok for the opportunity of integrating in his research project in Aalborg University and for his guidance and support throughout the development of this thesis. I would also like to thank Professor Kjeld Pedersen for giving me the chance to research for my master thesis in the Aalborg University.

In addition, a thank you to Peter Fojan, Muhammad Hanif and Peter Jensen, who not only assisted me with some steps of the fabrication and characterization process, but also helped me to overcome all the hardships found during the experiments.

To Professor Dr. Ana G. Silva, I would like to express my sincere gratitude. Thank you very much for the opportunity to do this thesis, for all the encouragement and support, for sharing all the knowledge in the long scientific discussions, the advices in all moments and the lovely week passed in Aalborg.

I would like to thank my friends for the support and motivation throughout my university years. To Pedro and Sofia who were with me since the beginning, to Flávia and Marta for the funny moments and support throughout these years (Pump the Jam!). To Mafalda and Lola, two stranger girls who shared a house with me in Aalborg, but since then they never left. And to Ricardo, the special guy who opened the door. Without them, these last years surely would not have been as fun as they were.

Finally, and most importantly, I would like to thank my family, my grandmothers Zica and Antónia, my uncle Miguel, my sister Carolina and specially my Mom and Dad. A big thank you for all the knowledge, encouragement, financial support, patience, laughs, and unconditional love that made all this possible.

Abstract

The phenomenon of localized surface plasmon resonance (LSPR) was used for detection of proteins incubated on size-selected silver clusters embedded in poly (methyl methacrylate) (PMMA) layers. The silver clusters were produced by magnetron sputtering and subsequently size-selected by electrostatic quadrupole mass spectrometer (EQMS).

The size-selection process was followed by the deposition of silver clusters with low kinetic energies, i.e. in a soft-landing regime on PMMA, in order to avoid the deformation and/or fragmentation of the silver clusters.

The role of PMMA hardness (viscosity) on cluster immersion was investigated to control the homogeneity in distribution of clusters, which can be partly or fully embedded in PMMA.

The viscosity of the polymers was found to be an essential part in the immersion of the silver nanoparticles into the polymer, which can be controlled through tuning of its viscosity or hardness utilizing simple thermal annealing of the samples.

The optical properties of the silver clusters - in particular the localized surface plasmon resonance (LSPR) – were measured with the optical absorption spectra of the silver clusters, in which was possible to clearly identify an intensity and a resonance band of the deposited clusters.

Proteins of interest were incubated on the clusters utilizing antibody-antigen scheme and clear change in the parameters of the LSPR band was observed allowing protein detection and demonstrating applicability of the fabricated composites in bio-sensing.

Keywords: Optical nano-biosensors; localized plasmon resonance

Resumo

O fenómeno de ressonância de plasmão localizado em superfície (LSPR) foi usado na detecção de proteínas em agregados de prata, de tamanho previamente selecionado e depositados em polimetilmetacrilato (PMMA).

Os agregados foram produzidos por pulverização catódica de magnetrão e subsequentemente selecionados em tamanho por um espectrómetro de massa do tipo quadrupólo electroestático, seguindo-se a sua deposição em PMMA em regime de baixas energias cinéticas (soft-landing), de forma a evitar a sua deformação e/ou fragmentação.

A dureza e a viscosidade do PMMA demonstraram ter um efeito relevante no controlo da imersão e homogeneidade dos agregados depositados, tendo por isso sido usados e testados diferentes tipos de PMMA.

As propriedades ópticas dos agregados – em particular a ressonância localizada do plasmão - foram obtidas medindo-se a sua absorção, tendo sido possível identificar claramente a intensidade e a banda de ressonância dos diversos agregados.

Como proteína de teste foi usada albumina de ovos de galinha. A ligação da proteína aos agregados é realizada utilizando a interacção química anticorpo-antigene. Foi comprovado com sucesso que a ressonância do plasmão se altera após ligação à proteína, demonstrando a sua aplicabilidade como um transdutor para um nano biossensor.

Palavras-Chave: Nano-sensores ópticos; Nano-física; Produção de agregados metálicos

Preface

The experimental work was carried out at the Department of Physics and Nanotechnology at Aalborg University, Denmark, for seven months in the spring of 2015. The purpose of this research was to produce and deposit metal clusters of silver on a quartz substrate with a thin film of PMMA and to characterize the samples using optical spectroscopy and AFM. The final goal of this thesis is to use the metal clusters as transducers for bio-nanosensors. The thesis was carried out under the supervision of Professor Dr. Ana Cristina Silva, Professor at Faculdade de Ciências e Tecnologia, Universidade Nova de Lisboa.

Contents

List of Figures

List of Tables

Glossary

AFM	Atomic force microscopy
E_{at}	Kinetic energy per atom
E_{coh}	Cohesive energy
E_{kin}	Kinetic energy
e	Charge of an electron
EQMS	Electrostatic quadrupole mass spectrometer
LSPR	Localized surface plasmon resonance
m_{eff}	Effective mass associated with the electrons move in response to the incident field
NHS	N-Hydroxysuccinimide
NP	Nanoparticle
n	Density of electrons in the bulk
PMMA	Poly (methyl methacrylate)
SCA	Spherical cluster approximation
SPR	Surface plasmon resonance
TEM	Transmission electron microscopy
ε_0	Free space permittivity
ω_p	Plasma frequency
γ_{Ag}	Surface energy of silver

γ_{PMMA}	Surface energy of PMMA
$\gamma_{interface}$	Surface energy in the interface of silver and PMMA
λ_{max}	Maximum Wavelength

1 Introduction

Biosensors with noble metal nanoparticles have been intensively researched in the recent years, contributing to the expansion of the biosensors market which is expected to reach $22.68 billion by 2020 [1]. The interest for this technology resides in their many advantages, in particular for optical biosensors due to their faster response, good selectivity, high sensitivity, low cost, and low interference with the phenomenon under study [2]. The technical advance of nano-biosensors in comparison with the traditional sensors has proven them to be an excellent tool with various applications in medical diagnosis, pharmaceutical and medical sciences [3,4], environmental monitoring [5], bio-recognition [6,7], bioprocessing and food quality control [8,9].

As generally defined, a biosensor is an analytical device with the ability to recognize the presence of a biological entity through a physical or chemical transducer and convert it into an output signal [10]. In 1960s, Clark and Lyons [11] proposed the idea of biosensors for the first time using an electrochemical sensor for glucose detection in blood plasma. This approach to the traditional mechanical sensors gave a new perspective for sensing biological materials.

According to the type of biological material , different techniques can be applied for its detection [12]. Amongst them, localized surface plasmon resonance (LSPR) biosensors have been an effective label-free tool for detection since the materials preserve their properties once they are detected in their natural forms [13]. Usually, the size of nanoparticles in these LSPR based sensors is similar to that of the organic molecules targeted for detection, such as enzymes and proteins, which makes them a good transducer for detection. Combining the nanostructure characteristics, the development of strategies for surface

bio-functionalization and the right bio-receptors to form nanostructure-biomolecules conjugates, LSPR sensing can achieve unique photonic, electronic and catalytic properties for biosensing.

In contrast with the surface plasmon resonance (SPR) technique, the LSPR provides a higher degree of sensitivity of the material to be detected [14]. However, some concerns in the fabrication of stable transducers must be considered in order to have an accurate and reliable response. Some of the most challenging tasks in fabricating and forming a stable transducer are held by the detection scheme design and surface immobilization chemistry.

One of the most widely used processes to obtain NPs is their production from colloids [15], even though this procedure results in particles with low stability and short shelf life times, leading to a rapid decay of their sensing properties. In this case, NPs are not usually size selected, i.e. there is a tendency to have particles of different sizes and many of them have the affinity to agglomerate with others. Another option to form NPs is through cluster beam systems [16,17]. In an earlier stage, this technique produces clusters in a gas phase, allowing for flexibility and precision in the control of the cluster beam composition and size. Afterwards, the clusters can be deposited on a substrate, which is carried out in high vacuum system. The versatility of this technique provides new application perspectives on nanostructuring of surfaces.

Real-time efficient detection of proteins of interest for several industries through the phenomena of localized surface plasmon resonance (LSPR) is optimized in the present work due to its novel immobilization studies and techniques for silver cluster deposition on polymer surfaces.

The novelty here lies on the deposition method, with the production of thin films of poly (methyl methacrylate) (PMMA) with good adhesion prospect of the nanoparticles (NPs). This procedure gave new perspectives for the NPs stability on samples, resulting in an advance in optical transducing technology, in contrast to the ones produced until now in colloids. Also, previous works on the formation of transducers for protein sensing using deposition of silver clusters on modified quartz surfaces were carried out [18].

2. Clusters and Cluster-PMMA Interaction

Clusters are usually described as small aggregates of atoms or molecules that represent a state of matter that is intermediate between atoms and the solid or liquid state, with properties that depend strongly on the size, shape, material of the particle, and its environment [19]. The unique physical, chemical and electronic properties of the NPs are a result of the high surface-to-volume ratio in clusters when compared to their bulk counterpart [16].

Regarding the nature of the clusters, they can be subdivided in terms of their constituent atoms (metallic, non-metallic or semiconducting) and the nature of the atomic bonding in those clusters. Silver nanoparticles are chosen as the clusters material in this work due to their high free carrier concentrations, which allows the formation of surface plasmons. Usually, the structure and the atomic arrangement of clusters are more complex and changeable than a solid bulk. By adding one or a few atoms, it is possible to change the entire cluster structure. Since the clusters size can differ depending on the parameters used in their production, they are divided in different categories according to their size boundaries (Table I).

Table I – Size regimes for silver clusters according with the definitions made by Johnston [19].

Cluster size regimes:	Sub nano-meter	Small	Medium	Large		Bulk
Number of atoms in a cluster		10	10^2	10^4	6.1 x 10^4	10^7
Cluster radii (Å)		4	10	40	65	400
$F_c = N_s/N$		1.85	0.86	0.19	0.10	0.02

In Table I, N represents the number of atoms in a cluster, N_S the number of atoms at the clusters surface and F_C is the fraction of atoms at the surface regarding the total number of atoms. Also, in Table I, the clusters size regime is represented by a grey scale, which is usually not well defined due to the complexity of determining a defined boundary for the clusters size, often differing in the literature [19-21].

2.1.The spherical cluster approximation

Clusters theory is described by several theoretical models which differ essentially on their applicability according to the cluster size regime and the nature of the atoms forming the clusters. Regarding metal clusters, the spherical cluster approximation (SCA), [19], the liquid drop model (LDM) [22,23] and the Jellium model [24], are some of the models that provide reliable approaches to study the clusters properties, depending on their size, geometry and shape.

For the clusters produced in this work, the model of the spherical cluster approximation (SCA) [19] is a good approach that considers a cluster sphere composed of N atoms, with cluster radius R_c and total volume V_c.

The clusters volume is given by the volume of an atom multiplied by the number of atoms in the cluster, $V_c = V_a N$. N can be expressed in terms of the cluster and atomic radii, where for a single atom the volume will be V_a and the radius R_a.

$$R_c = N^{1/3}\, R_a \tag{2.1}$$

The cluster surface area S_c can be described as a function of the total number of atoms N in the cluster. For a single atom, with a surface area of $4\pi r^2$, it yields:

$$S_c = 4\,\pi R_c^2 = 4\,\pi \left(N^{1/3}\, R_a\right)^2 \tag{2.2}$$

The number of atoms on the surface, N_s, is determined by dividing the surface area of the cluster by the cross section of an atom in the cluster, πR_a^2:

$$N_s = \frac{4\,\pi N^{2/3}\, R_a^2}{\pi R_a^2} = 4\, N^{2/3} \tag{2.3}$$

The fraction of atoms on the surface of the cluster, F_c, is simply related to the total number of atoms in the clusters:

$$F_c = \frac{N_s}{N} = 4\, N^{-1/3} \tag{2.4}$$

The relation in equation (2.1) will be used in this work to calculate the number of atoms in the clusters. Considering the mean radius for size-selected silver clusters produced, $R_c \approx 6.5$ nm, with the Wigner-Seitz atomic radius of silver, $R_{WS} = 1.66$ Å [25], the number of atoms N in the cluster using the SCA will be:

$$N = \left[\frac{R_c}{R_{WS}}\right]^3 \approx 6.11 \times 10^4 \text{ atoms}, \tag{2.5}$$

which will represent a fraction of atoms on the surface of the cluster of $F_C = 0.10$, meaning that the amount of the surface atoms is $N_S = 6160$ atoms. Also, regarding Table I, the clusters size regime where the produced silvers clusters are situated is between the large and the bulk regime.

2.2.Fundamental aspects of cluster nucleation and growth

The main aspects in the clusters formation are the nucleation (formation of a dimer as a nuclei) and the growth (larger than a dimer) processes [16]. The nucleation process is difficult to control and requires special conditions for the formation of clusters, since the experimental tools used are not capable of capturing, identifying and monitoring the nuclei. The nucleation process can be understood in terms of the kinetics of the formation of the initial NPs followed by their interaction in vapour form [26].

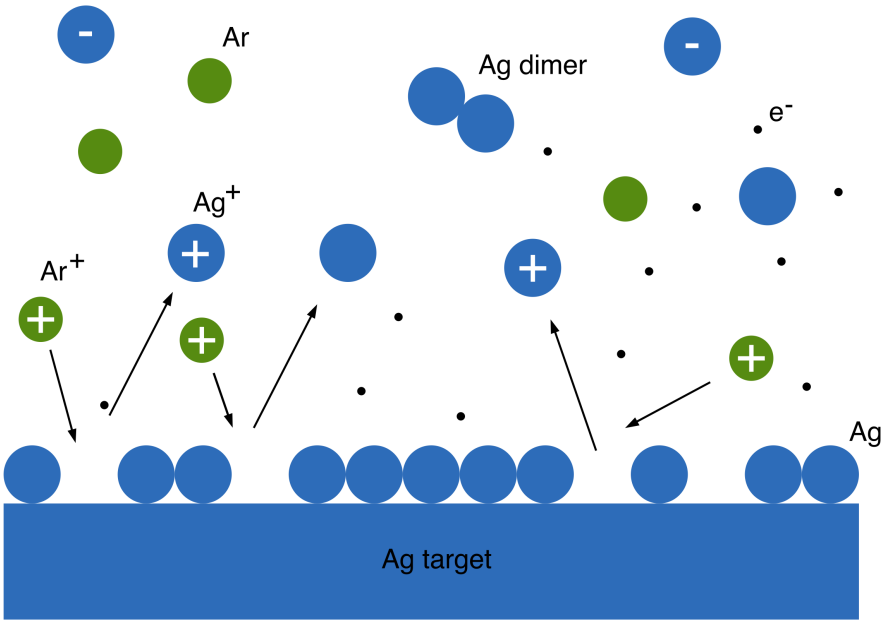

Figure 1 – Schematic of the sputtering process of silver nucleation in dimers. The units – circles – represent atoms and ions, while dots represent electrons. The smallest cluster is the silver (Ag) dimer.

In this work, silver atoms are obtained by sputtering a silver target with argon (Ar) ions, usually known as the sputtering gas (Figure 1). From the sputtering process, positive and negative silver ions can be obtained as well as neutral atoms. Usually, negative ions are obtained in a higher percentage [27]. The nucleation occurs when at least metal atoms/ions collide with each other involving a third particle (Ar) to absorb the excess energy released at the nucleation. The chemical reaction and the three-body collision process can be represented as the following equation:

$$Ag + Ag + Ar \rightarrow Ag_2 + Ar \quad (2.6)$$

After the nucleation (the smallest cluster/nuclei), clusters will enter in the aggregation zone with specific experimental conditions such as temperature and pressure, leading to clusters with different sizes and thermodynamically stable.

For the growth of clusters, different independent processes can occur (Figure 2), including atom attachment, coagulation (kinetic and diffusion modes), coalescence and aggregation [21,26]. The size of clusters will depend on the time the clusters stay in aggregation zone, where longer times lead to larger clusters. The size distribution of the clusters is also dependent on the charge of the clusters and on the ratio of positive to negatively charged particles.

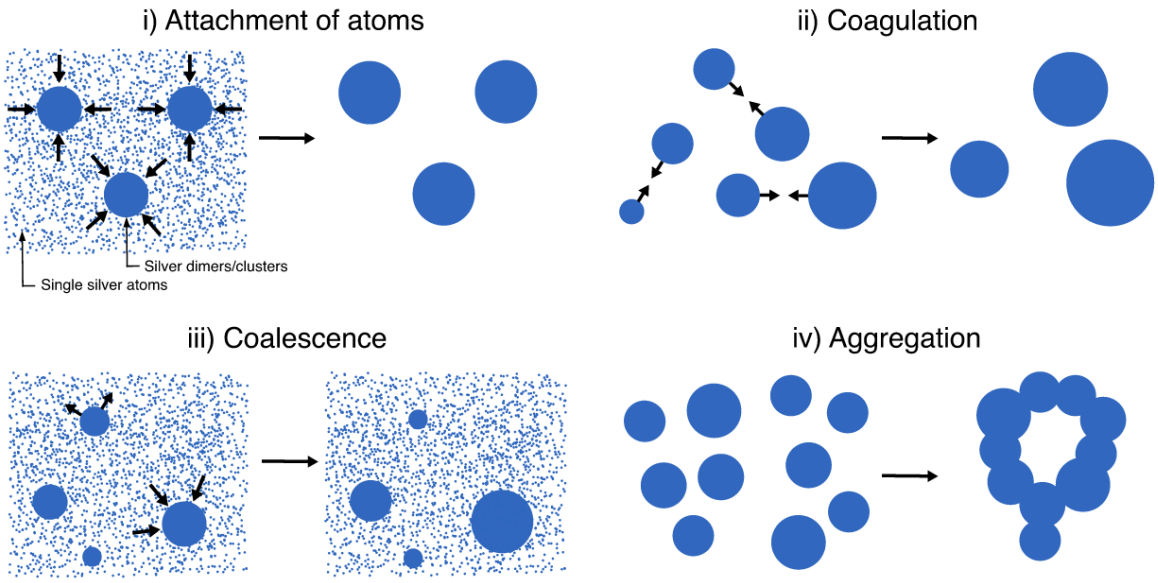

Figure 2 – Schematic of the different processes of the clusters growth on the aggregation zone of the chamber, including the i) attachment of the atoms, ii) coagulation, iii) coalescence, and iv) aggregation of the silver clusters.

During the attachment process (Figure 2 i)), silver single atoms/ions become attached to the clusters Ag_n $(n \geq 2)$ already formed [26]:

$$Ag_n + Ag \rightarrow Ag_n + 1 \quad (2.7)$$

This process can occur at any instant of time in the aggregation zone of the chamber. Some of the atoms attached to dimers and clusters formed by this process have less stability than the dimers formed during the nucleation process (Figure 1), due to the transfer of additional energy from the attachment to the buffer gas (Ar) [28].

The coagulation process is the formation of larger clusters from two individual clusters of smaller sizes (Figure 2 ii)). This process can happen in two different regimes, kinetic and diffusion regimes, which is directly dependent on the Brownian motion of the buffer gas in the aggregation zone, allowing the interaction between the atom and the cluster. In the kinetic regime, only single atoms or molecules can interact with the cluster, while in the diffusion regime many atoms interact simultaneously with the cluster.

Coalescence results from the interaction of clusters with a parent vapor and it only occurs for the very low degree of supersaturation. For smaller clusters, the rate of atom evaporation is higher than the rate of atom attachment, while for larger clusters the inverse relation is observed (Figure 2 iii)). As a result, large clusters grow while small clusters evaporate. Coalescence depends on the critical cluster size or radius for equilibrium with a parent gas or vapor.

Aggregation is a process where the individual clusters are joined due to their contacts while retaining much of their original shape [26]. This process results in the fractal growth of clusters (Figure 2 iv)).

2.3.Clusters PMMA interactions

In this section, it is presented an overview of the interaction process between silver clusters and a PMMA thin film deposited on quartz. Depending on the used type of cluster source, two different regimes for clusters deposition can be verified, depending on the kinetic energy of the generated cluster flow [29] (Figure 3).

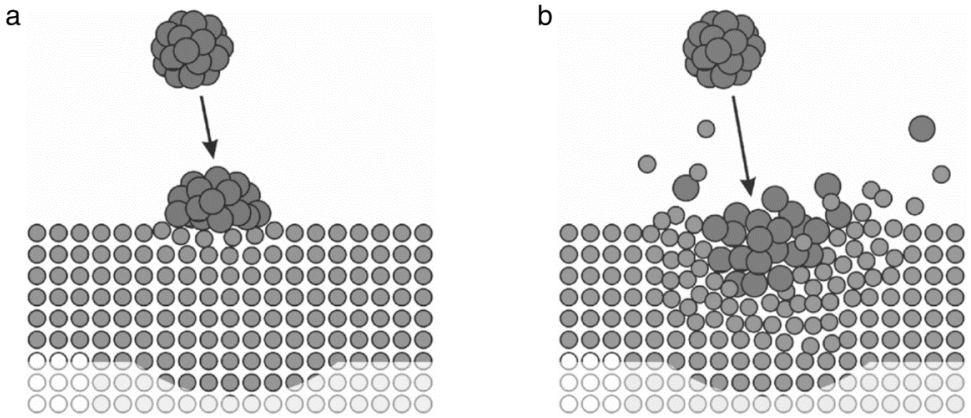

Figure 3 – Schematic of the two cluster beams kinetic regimes, with (a) cluster soft landing and (b) cluster-surface high-energy impact [29].

The surface properties of the Ag clusters, in particular those affecting the plasmon resonance, are very much dependent on their interaction with the PMMA surface and how they become, partly or fully, embedded into a surface, thus being of great importance a precise control during their deposition, the kinetic energy E_{kin} of the clusters is then an important parameter during the deposition, to establish the appropriate regime of the cluster-surface interaction, distinguished into low and high energy [29].

In the case of low-kinetic energy (Figure 3a), which is the impact regime considered in this work, the kinetic energy per atom (E_{at}) is lower than the cohesive (or binding) energy (E_{coh}) of the cluster constituents, which is typically around $E_{at} \approx 0.1\ eV/atom$ [29]. Moreover, in the soft-landing regime the cluster fragmentation is greatly reduced, preserving their decomposition, even though their structure/shape can be distorted due to the impact.

If E_{at} is close to E_{coh}, or if the atoms of the deposited cluster strongly interact with the substrate atoms, the clusters can face a plastic deformation. Otherwise, if the E_{at} exceeds E_{coh}, the impact is of high-energy, and according to E_{at} and E_{kin}, the clusters can be plastically deformed, fragmented and/or implanted.

The embedment of clusters, partly or fully, is dependent on the PMMA surface and cohesive energies of the constituents. By annealing the PMMA, the bulk structure and cohesive energy can change, offering more or less resistance to the penetration of the clusters. In this work, *hard*, *viscous* and *soft* PMMA, annealed at different temperatures, were used.

In order to achieve the complete embedding of a cluster into a polymer, the different energies involved should obey to the following relation [30]:

$$\gamma_{Ag} > \gamma_{PMMA} + \gamma_{interface}, \tag{2.8}$$

where γ_{Ag} and γ_{PMMA} are the surface energies of the silver cluster ($\gamma_{Ag} \approx 1200$ mJ/m^2) and polymer ($\gamma_{PMMA} \approx 30 - 40$ mJ/m^2) [31], respectively, and $\gamma_{interface}$ is the cluster-polymer interfacial energy. This condition is usually satisfied for metal clusters on a polymer, since metals generally have surface energies two orders of magnitude higher than the polymers, and thus complete embedding is expected.

The embedding of a metal cluster depends also on the chain mobility changes of the polymer induced when clusters are deposited, which is only verified by tuning the viscosity/hardness of the polymer. Depending on the annealing temperatures of the PMMA, a total, partial or no embedding of the silver clusters can be expected.

For PMMA, it is expected that for temperatures above the glass transition temperature, $T_g = 105$℃ [31], silver clusters deposited in a soft-landing regime will stay at the surface, since the kinetic energy of the silver clusters is lower than cohesive energy of the polymer.

The kinetic energy of each atom used in this work can be determined by the expression:

$$E_{Ag} = \frac{m_{Ag}\, v^2}{2}, \tag{2.9}$$

where the atom mass of silver is $m_{Ag} = 108{\times}1.67{\times}10^{-27}$ Kg and v is the velocity of the silver NPs, $v \approx 200\ m/s$. As such, the energy of a silver cluster can be of the order of:

$$E_{Ag} = 3.6 \times 10^{-21}\text{J} = \frac{3.6 \times 10^{-21}\text{J}}{q} = 22.5\ \text{meV},$$

resulting in a kinetic energy for each cluster of $E_C = N\, E_{Ag} \cong 136$ eV.

This kinetic energy will characterize the deposition regime, and the dependence for the clusters embedment will rely only on the thermal annealing of the PMMA, which will be discussed on Chapter 5.

3. Plasmonic Sensing

The moment where a beam of light traveling through a dielectric (air, water, glass) reaches a surface of a conducting material creates a traveling wave at the metal-dielectric interface, due to displacement of the electronic cloud [32]. This wave is commonly referred to as a surface plasmon, with a natural plasma frequency (ω_p) at which the oscillation occurs, that is defined as:

$$\omega_p = \sqrt{\frac{ne^2}{\varepsilon_0 m_{eff}}} \tag{3.1}$$

where n is the density of electrons in the bulk, m_{eff} is the effective mass which is associated with the electrons move in response to the incident field, e is the charge of an electron and ε_0 is the free space permittivity.

The plasmon frequency is not a single resonant frequency associated with the electrons in the bulk of the metal. Instead, the motion will be based on whether the electrons can respond quickly enough to the driving force of the incident field. If the frequency of the incident field is different than ω_p, most of the incident light will be scattered.

However, if the incident field is equal to ω_p, i.e. the natural frequency of the oscillation, the incident light will be absorbed by the oscillation, thereby enhancing its amplitude which results in the plasmon resonance of the bulk material, also known as surface plasmon resonance (SPR).

To fulfill the resonant condition, SPR should respect the momentum conservation of the system. Due to the differences between the momentum of the incident light and the surface plasmon, the resonant condition can be achieved through adaptive optics to increase the momentum of light. These surface plasmon waves will be confined only to flat

surfaces and they can only be excited by using special geometries required for matching the wave vector, k_{sp} when producing the plasmon wave. However, when using metal nanoparticles, the plasmon oscillations will be localized, as it will be explained in the following section.

3.1.Localized surface plasmon resonance

When a surface plasmon is confined to a particle with a size much smaller than the wavelength of the light emitted, the particle's free electrons will have a collective oscillation, resulting in the so called localized surface plasmon resonance (LSPR) presented in Figure 4 [32]. The electric field near the particles' surface is greatly enhanced due to the formation of surface plasmons and the intensity will decay exponentially with the distance (evanescent waves).

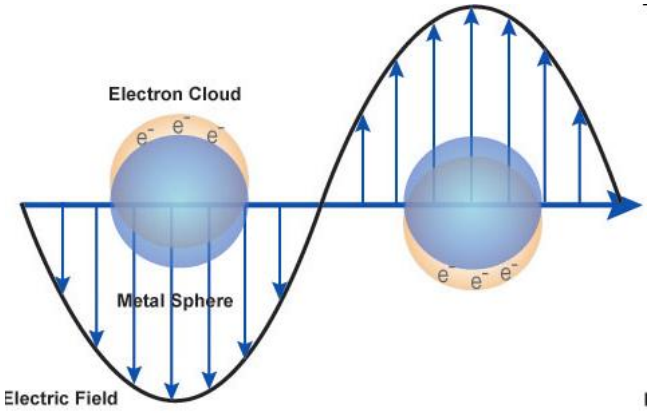

Figure 4 – Schematic of plasmon oscillation for a metal NP, showing the displacement of the conduction electron cloud about the core or nuclei, due to strong coupling with incident light [33].

This phenomenon occurs in noble metal NPs with dimensions (10-150 nm) much smaller than the wavelength of incident light (400-900 nm). These NPs have extraordinary optical properties that are not exhibited by any other class of material, being unique depending not only on the morphology of the NP but also on the environment it is subjected to. By changing the size, shape and material composition of the NP, the sensing capability of the LSPR can be tuned. Once these resonances are excited, absorption and scattering intensities can be up to forty times higher than identically sized particles that are not plasmonic.

As a result of the induced plasmons oscillating locally to the nanostructure (LSPR) rather than along the metal-dielectric interface (SPR), the decay length of the electromagnetic field (EM) observed in localized surface plasmons is in the order of δ_{LSPR}~6 nm [34] (Figure 5 ii)), and by comparing to surface plasmons of δ_{SPP}~200 nm [35] (Figure 5 i)), one can say that LSPR frequency is highly sensitive to the refractive index of the environment, where a change in refractive index results in a shift in the resonant frequency. This shift is easily measurable, which allows the use of metal nanoparticles for sensing applications on the nanoscale. The shorter field decay length for LSPR provides a sensitivity increasing of the refractive index changes on the surface.

The complexity of LSPR technology resides in the surface of the chip since the instrumentation used to read the signal is quite simple. In sharp contrast, the complexity of SPR resides in the precise setup of the instrumentation to launch a surface plasmon and read it accurately. In biosensing applications, the differences between SPR and LSPR become specifically notable, namely the sensing volume of their respective plasmons captured by what is referred to as bulk effect (Figure 5).

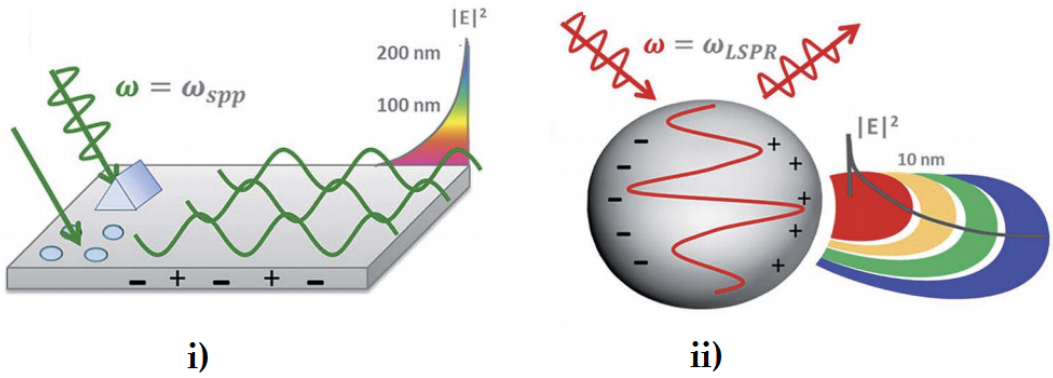

Figure 5 – Surface (i) and localized (ii) surface plasmon resonance phenomena. On the right side of (i) and also in (ii) can be seen the exponential decay length of the EM field from the interface. Adapted from [13]

Due to the much larger plasma field of SPR, even biomolecules that are not actually bond at the sensor surface can be detected, causing a bulk effect or false positive reading. Therefore, SPR has not been successfully applied in the diagnostic field, such as blood-based immunoassays, as the detection of low-level biomarkers requires signal amplification.

In contrast, LSPR can only sense the molecules bound at the surface of the biosensor, while the other ones are invisible and do not contribute to the signal. However, LSPR has a marginal bulk effect due to the small size of the localized plasma evanescent field.

3.2.Optical properties of nanoparticles

In 1908 Gustav Mie [36] obtained the exact solutions to Maxwell's equations of the macroscopic electromagnetism which can be applied to describe LSPR. The solution for the electromagnetic scattering considers a nanosphere of radius R embedded in a homogeneous and isotropic medium illuminated by a plane wave.

The scattered field and the field inside the particle can be obtained from the incident field by applying the boundary conditions between the nanosphere and the medium at the surface of the nanosphere by considering a linear, isotropic and homogeneous medium and a polarized incident wave plane.

With Mie's formulation, one of the simplest way to calculate the extinction coefficient of a metal nanosphere in LSPR can be represented by Q_{ext}, and dependent on the dimension, shape, density and local environment of the nanostructure [37]:

$$Q_{ext} = \frac{24\,\pi R \varepsilon_{med}^{3/2}}{\lambda}\left[\frac{\varepsilon_{im}}{(\varepsilon_r + 2\varepsilon_{med})^2 + \varepsilon_{im}}\right] \tag{3.2}$$

where R is the radius of the nanosphere, ε_{med} is the relative dielectric constant of the medium surrounding the nanosphere (the dielectric constant is assumed to be a positive, real integer and wavelength independent), λ is the wavelength of the absorbing radiation, ε_r and ε_{im} are the real and imaginary parts of the metal nanoparticle dielectric constant, respectively [5].The extinction coefficient measures the rate of transmitted light via scattering and absorption for a medium.

The equation (4.2) shows that the interaction between a metal nanoparticle and the incident light depends strongly on the dielectric properties of the metal nanoparticle (ε_r and ε_{im}). If the denominator of the bracketed expression approaches zero, Q_{ext} will become extremely large and at this frequency the optical absorption and scattering will also be exceedingly strong. For that, the ε_r must be close to $2\varepsilon_{med}$.

For the size-selected silver clusters produced with $d \approx 13\ nm$, the optical extinction has a maximum at the plasmon resonance frequency, which occurs at 413 nm. Due to interactions between the incident photons and the conduction electrons band of a noble metal nanostructure, a collective oscillation of the electrons and subsequent absorption within the ultraviolet visible (UV-Vis) band is generated.

3.3.Localized surface plasmon resonance in biosensing

One of the main applications of LSPR in biosensing is the detection of small molecules. As bio receptors (e.g. enzymes, antigens and antibodies) have dimensions in the range of $2 - 20\ nm$, similar to those of nanostructures, the two can be considered structurally compatible. This dimensional compatibility means that highly miniaturized signal transducers can be achieved through the combination of nanostructure characteristics, a wide selection of available bio receptors and the rapid development of surface bio-functionalization strategies.

The first step when designing a LSPR biosensor is to choose the nanostructure-biomolecule conjugates. As mentioned before, noble metal nanostructures have unique photonic, electronic and catalytic properties. By functionalizing these nanostructures with biomolecules, such as proteins or DNA, novel substrates can be developed to be used in different biomedical applications, such as sensing, imaging, diagnosis and therapy.

LSPR has been experimentally shown to be highly sensitive to several structural factors, such as dimension, shape and spacing, as these factors impose requirements in the fabrication of the sensor substrates for reliable and repeatable measurements. Figure 6 illustrates the effect that the nanostructure can have on the extinction wavelength maximum ($\lambda_{\max}$) for different shapes of a nanostructure.

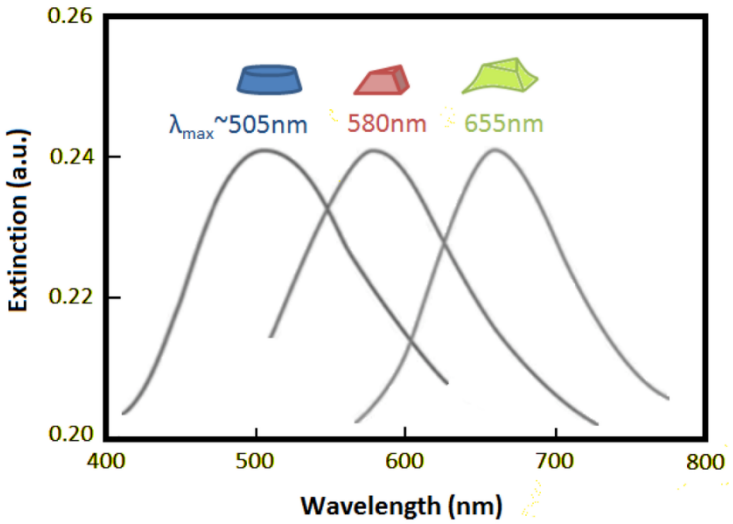

Figure 6 – Diagram illustrating how the nanostructure shape affects the extinction wavelength maximum (λ_{max}) [38].

LSPR spectroscopy offers sensing through transduction of refractive index changes in close proximity to the surface of the noble metal nanoparticle. Formation of adlayers (adsorbate layers that are chemically interacting with the subtract) and biorecognition

events on the surface cause quantifiable shifts in the LSPR extinction wavelength maximum, λ_{max}, due to the dependence of the adlayer refractive index, n. The refractive index is related to the dielectric constant by $n = \varepsilon^{1/2}$, as demonstrated by:

$$\Delta\lambda_{\max} = m\Delta n\left[1 - \exp\left(-\frac{2d}{l_d}\right)\right] \tag{3.3}$$

where m is the bulk refractive index response of the nanostructure, d is the effective adsorbate layer thickness and l_d is the characteristic electromagnetic field decay length, modelled as an exponential decay [35]. The binding kinetics can then be monitored by tracking $\Delta\lambda_{\max}$ as a function of either time or analyte concentration [37].

4. Experimental Methods

This chapter describes the experimental procedure followed in this work, where the process to form the silver clusters is explained, as well as all the steps to obtain the nanosensors.

4.1. Clusters Production

Regarding the production of clusters, there are several techniques and procedures that can be applied. They depend on the experimental setup used in the cluster apparatus, which is usually composed by a production, a mass selection (if required) and a detection section.

Some fundamental requirements regarding the cluster material, size and energy distribution, overall cluster electrical charge, must be taken into consideration during the design of the experimental setup. In a first approach, it is necessary to choose an efficient clusters' source with the required parameters to produce the desired clusters.

There are a vast number of sources used in the production of clusters, such as the supersonic nozzle (free jet), gas aggregation, surface erosion, thermospray, and electrospray sources [16]. In this work, a magnetron sputtering source is used to produce the size-selected silver clusters. This technique provides several advantages during the production and deposition steps, such as precise control of the composition and size of the clusters produced, the surface coverage, and the kinetic energy, which defines the cluster surface interaction.

4.1.1. Magnetron Sputtering

The magnetron sputtering cluster apparatus (MaSCA), presented in Figure 7, was used in the production and deposition of the silver clusters. The system consists of several vacuum chambers that can be defined by two different regions.

The red region presented in Figure 7 contains the magnetron where the material target is placed. In this region, a silver target is sputtered with a subsequent aggregation of this material into clusters. The left region of this chamber includes the ion optics chamber, where the beam of silver clusters will be collimated and then selected in size by the electrostatic quadrupole mass selector (EQMS), leading to their deposition on a sample.

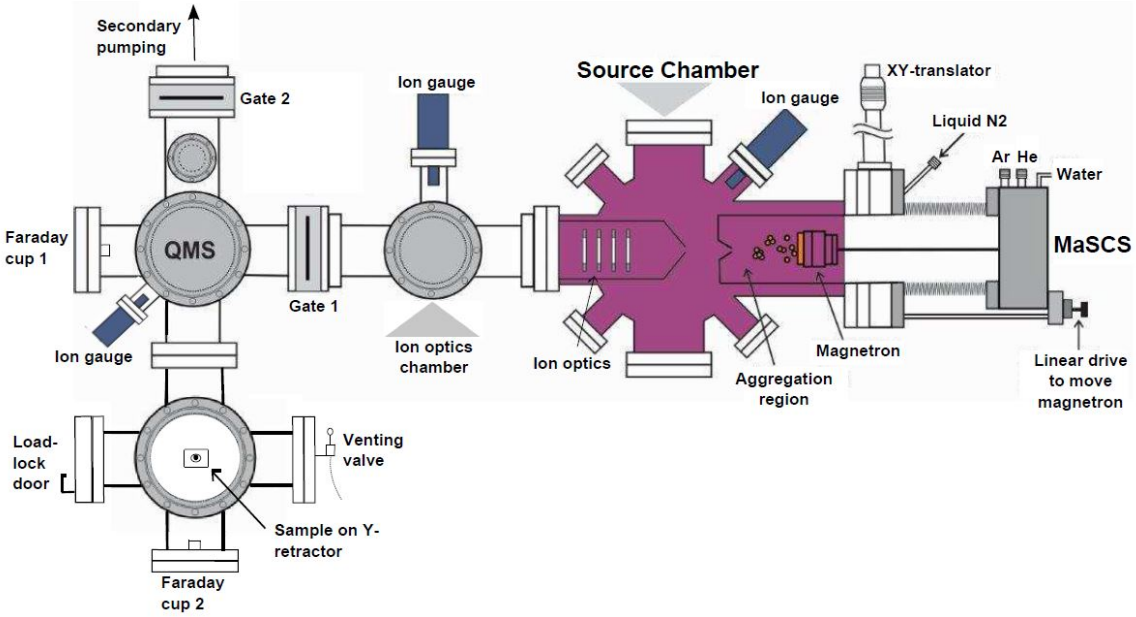

Figure 7 – Schematic of the system used for the production and deposition of silver clusters [39].

The key part of a MaSCA system is the commercial source (NC200U from Oxford Applied Research) composed by a DC magnetron that allows the sputtering of a metal target by the Ar plasma. A silver target of 99.99% purity (from Good Fellow Ltd) is used to produce the silver clusters. The magnetron sputtering source is connected to the source chamber by the manipulator, allowing a 3D alignment of the source.

The linear translation in the range of $l \approx$5-100 mm is very important here since it allows to vary the aggregation lengths that in turn affects the size of the formed clusters as well as the cluster beam intensity. For short aggregation lengths, the clusters produced will be smaller due to the fewer number of collisions, meaning that, the aggregation length must be increased to obtain larger clusters.

Figure 8 shows the magnetron sputtering system, with a detail of the magnetron head (Figure 8 i)), where it can be seen the silver target already eroded by the sputtering

gas (Ar). Also, in Figure 8 ii) the linear translation is visible below the magnetron, as well as the gas flow system (sputter and aggregation gases) and the cooling system.

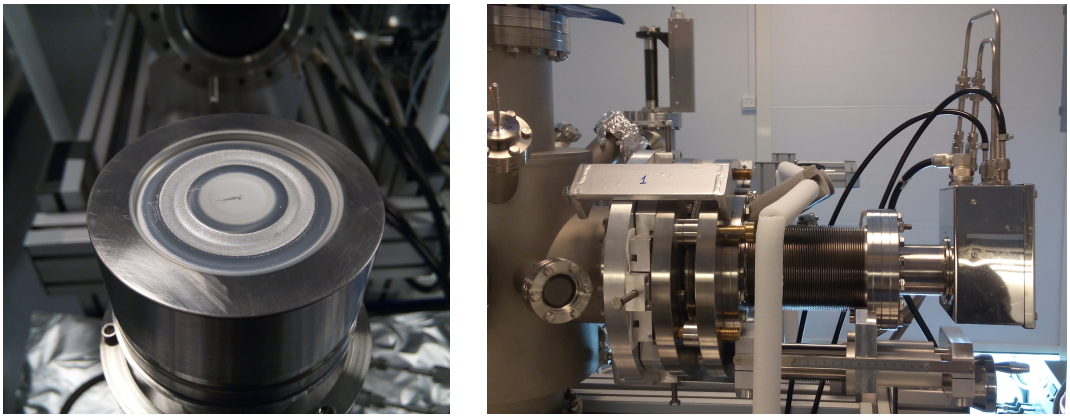

i) ii)

Figure 8 – Magnetron head with the silver target already eroded by the sputtering gas (i)), composition of the magnetron sputtering on the aggregation chamber, with the cooling system and the gas flow circuit (ii)).

Using Ar and He (regulated by two gas flow controllers) as the sputter and aggregation gases, respectively, the silver target is sputtered and the clusters are aggregated. By varying the discharge power, the flows of sputtering and aggregation gases, and the aggregation length in the source, one can adjust the clusters size and the beam intensity.

The differences between the pressure in the aggregation and source chamber generates an expansion through a nozzle into the source chamber creating a flow of charged silver clusters. The diameter of the nozzle is another important parameter to optimize the expansion process, which can vary from 1 to 5 mm (Figure 9).

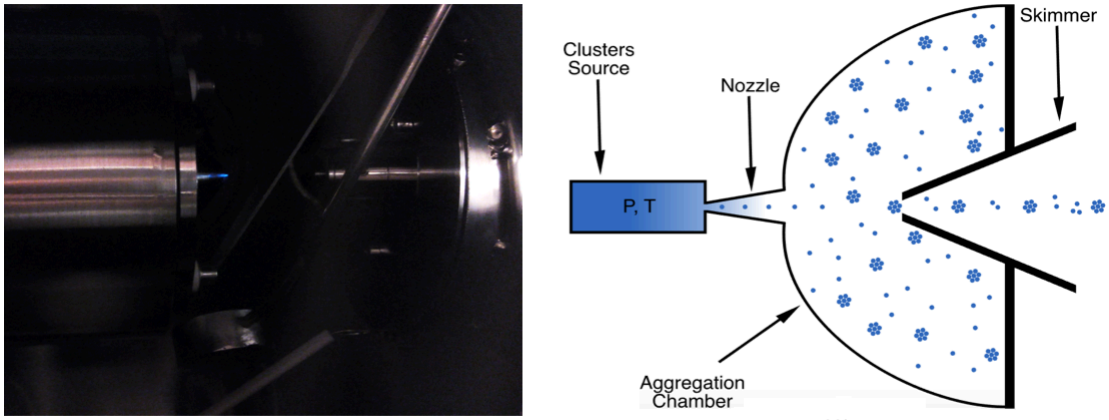

i) ii)

Figure 9 – Nozzle-skimmer configuration inside the source chamber (i)), where is visible the reflection of the plasma formed in the aggregation chamber in the skimmer. The schematic representation of the production of silver clusters in (ii)

Inside the source chamber (pumped by a 1250 l/s turbomolecular pump), a skimmer is mounted at the entrance to the ion optics chamber with a 2 mm orifice which allows a collimated beam. The ion optics chamber (pumped by a 355 l/s turbomolecular pump) contains an Einzel lens and two pairs of deflectors to adjust the beam direction.

The pressure in the ion optics chamber is reduced about two orders of magnitude when compared to the source chamber, reaching typically 10^{-4}-10^{-5} mbar. Between the EQMS and the ion optics, a gate valve is mounted that allows to isolate EQMS and deposition chamber from the source. The parameters are optimized to direct the beam into the entrance orifice of the EQMS, allowing the size-selection of the clusters, which will be described in the following section.

4.1.2. Size-selection of clusters

One of the main concerns inherent to the clusters production is the size distribution, therefore it is imperative to have it into account for a practical application. The clusters expanded from the nozzle are assumed to have nearly the same velocity. A significant fraction of the produced clusters is ionized. Therefore, to achieve mass filtering, EQMS is used.

The EQMS is composed by electrodes of 120-mm-long quarter cylinders and are divided into two pairs that are biased with the same absolute voltages, U_{QP}, up to 5 kV but with opposite polarity. The electrodes are surrounded by a grounded shield with circular orifices for the cluster beam, where the orifices are covered by metal grids to minimize field penetration. Detailed description of the principle of operation of EQMS can be found elsewhere [27]. In brief, the EQMS consists of four electrodes (represented by red and yellow in Figure 10) that create an electrostatic field.

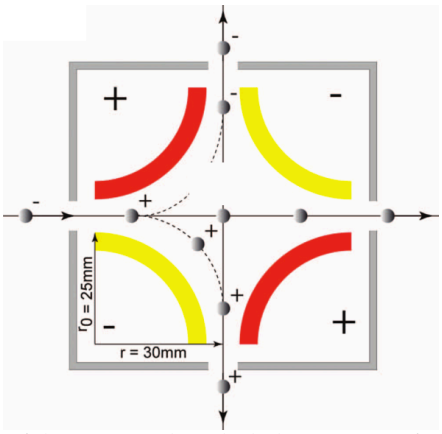

Figure 10 – Cross-sectional view of the QMS with included trajectories for positive, negative and neutral clusters, respectively [27].

By varying the applied potential, it is possible to change electrostatic energy to make it match the kinetic energy of the clusters with a given mass. Thus, only clusters with this mass will be deflected 90° to enter the deposition chamber (Figure 10). For the EQMS used, the diameter of the clusters can be selected with ± 5-7% precision. It has been proved clusters can be produced (but not limited) with diameters between ca. 5-25 nm [40].

One of the requirements for the setup is the ability to deposit clusters under high vacuum conditions, therefore, the deposition chamber is equipped with a 230 l/s turbo-molecular pump that allows for a background pressure of ≈ 10^{-8} mbar. Two faraday cups are used for beam monitoring: one in the main axis direction of the cluster source to measure the clusters current produced by the MaSCA, and another one in the deposition chamber to measure the current of the size-selected clusters deflected by the EQMS and intended for the deposition on a substrate.

The parameters for cluster production presented in Table II were interrelated by many parameters which are typically varied for optimizing the beam intensity to obtain the desired cluster size.

Table II – Clusters flow of the sputter and aggregation gases (Ar and He respectively) depending on the clusters size desired.

Clusters Size	F_{Ar} **(sccm)**	F_{He} **(sccm)**
Small	40 - 60	10 - 20
Large	50 - 65	2 - 10

The beam intensity, which depends on the kinetic energy of the NPs, also affect the sputtering power and gases used in the clusters formation. An additional parameter that affects the cluster's size is the distance between the target and the nozzle (aggregation length, Figure 9 ii)), where a shorter aggregation length leads to smaller clusters due to the reduced number of collisions.

4.2.Nano-biosensors Synthesis

Before the deposition of size-selected clusters on substrates, a thin film layer of PMMA were deposited on silicon (Si) and quartz substrates by a standard spin coating equipment (model WS-650-23B from Laurell Technologies Corporation) from 1% solution of PMMA (molecular weight 950K PMMA C 9, MicroChem, America) diluted in toluene.

The thin films were produced at the exactly same conditions for both types of substrates in order to measure the PMMA thickness on Si by ellipsometry and use this value as a reference for the PMMA thickness on quartz substrates.

In the current experiments, PMMA thickness varied between 10-100 nm depending on the parameters used on the spin coater (time, rotations per minute, and acceleration). Silver clusters of a given size (ca. 13 nm in diameter) were deposited on PMMA of different hardness and subjected to post-deposition thermal annealing to study immersion of particles into the polymer.

Three types of PMMA films were prepared on quartz according to their annealing temperatures:

- **(i)** *Hard* PMMA was annealed at temperatures quite above the glass transition prior the cluster deposition;
- **(ii)** *Viscous* PMMA was only dried at ambient conditions prior the cluster deposition, thus, having low hardness that facilitates the cluster immersion;
- **(iii)** *Soft* PMMA was annealed at temperatures below the glass transition (100℃) prior the cluster deposition.

These samples were tested as optical transducers to study the possibility of protein detection. Table III shows the preparation conditions of the PMMA thin films used for the deposition of the size-selected silver clusters.

Table III – Preparation conditions of the *hard*, *viscous* and *soft* PMMA samples.

Samples	**PMMA**		**Annealing**		
Ag/PMMA/Q	**Thickness (nm)**	**Type**	**Nº of annealing**	**T (℃)**	**t (min)**
# 09	54	*Hard*	1	180	30
# 10	100	*Hard*	1	180	30
# 19	20	*Viscous*	2	95	30
				115	15
# 16	100	*Viscous*	2	95	5
				100	10
# 18	10	*Soft*	4	95	10
				100	30
				100	30
				115	15
# 17	70	*Soft*	3	95	10
				100	30
				115	15

After the initial characterization by AFM and optical spectroscopy, the samples which were qualified for protein sensing (i.e. with a high clusters density immobilized in the PMMA layer, giving a typical plasmon resonance peak for silver clusters) will be submitted to all the steps in the building of a functional transducer for nano-biosensing, i.e. the functionalization of the samples surface through MUDA and their activation (EDC/NHS) for the deposition of proteins of interest (antibody, antigen). Table III shows all the selected samples that meet the requirements for protein sensing.

A schematic of the experimental procedure to obtain stable transducers for protein sensing is presented in Figure 11. The production of size-selected silver clusters is followed by their deposition in a quartz substrate with a thin film of PMMA on top.

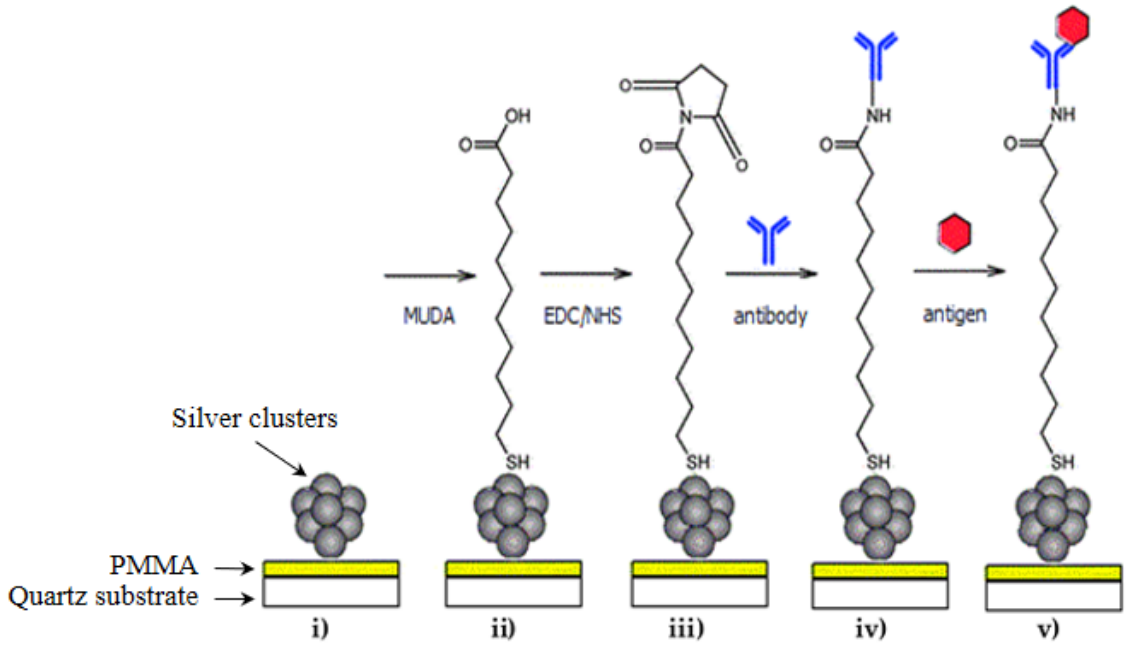

Figure 11 – Schematic of the steps for the production of transducers for protein sensing, adapted from [41].

In order to have a stable and strong binding of the biomolecules to the NPs, a functionazilation of the clusters surface must be carried out. For that, substrates with as-deposited clusters were incubated in a solution of 10mM 11-Mercaptoundecanoic acid (MUDA) with 98% purity (from Sigma-Aldrich) diluted in 96% of ehtanol for 30 min, resulting in a formation of a self assemble monolayer (SAM) on the samples (Figure 11 ii)). Subsquently, the samples were washed with ethanol to remove the residual and not reacted MUDA and dried under a stream of nitrogen.

MUDA (Figure 12) becomes selectively bond to silver clusters via the sulphur-containing end (HS) and its carboxyl group (COOH) provides a covalent amid bond to the antibodies that will be deposited in the transducer.

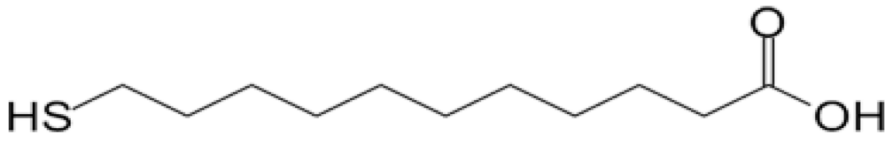

Figure 12 – Chemical formula of 11-Mercaptoundecanoic acid (MUDA).

However, to form a bond between the functionalized NPs with MUDA and with the antibodies, a carboxyl activator agent should be present to bind the biomolecules to the NPs. For that, the samples were incubated with a freshly prepared solution of 40mg/mL 1-ethyl-3-[3-dimethylaminopropyl]carbodiimide hydrochloride (EDC) (Figure 13 i)) and

10 mg/mL N-Hydroxysuccinimide (NHS) (Figure 13 ii)) in 1 mL of deionised water for 20 min. Subsequently the sample was washed with deionised water and dried under a stream of nitrogen.

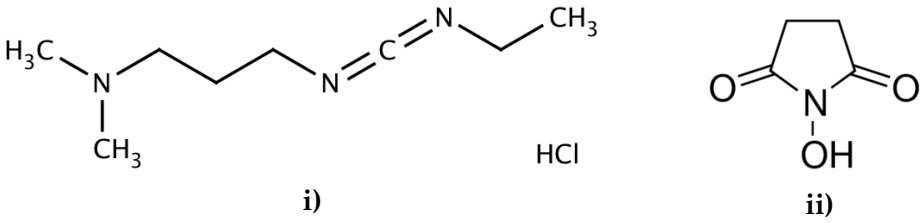

i) ii)

Figure 13 – Chemical formula of EDC (i) and NHS (ii)

EDC/NHS coupling will activate the carboxyl group (COOH) in MUDA, which will be used to form a covalent amide bond to the antibody [42]. The strong chemical bond will change the dipole characteristics of the silver clusters which will enhance the LSPR absorption. This process in represented in Figure 11 ii) and iii)). The EDC coupling reaction should be carried out fast for an efficient bonding between MUDA and the antibody, as the reactive ester (an acid that replaces hydroxyl group (-OH) by an alkyl (-O) group) that is formed can be hydrolysed in aqueous solutions [43]. NHS will be the agent that will give stability to this active ester from the EDC coupling.

Regarding the detection of biological material of interest with the LSPR phenomena, an antibody-antigen scheme was used to test the transducers produced. The detection consists of an anti-chicken egg albumin (antibody) and albumin chicken egg white (antigen), a schematic of the antibody-antigen binding is shown in Figure 14. These proteins are well characterized and understood in the literature and they only have the purpose to test the applicability of the developing detection approach for this work.

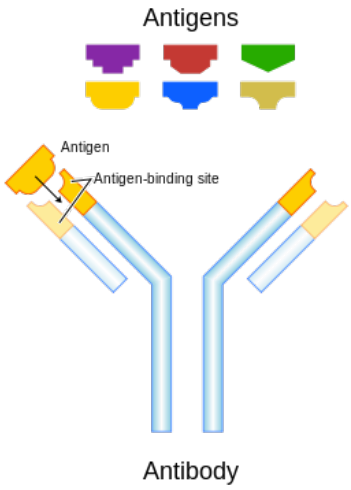

Figure 14 – Schematic of the antibody antigen binding [44].

For the protein deposition, a 10 mM solution of chicken egg albumin (antibody) (from Sigma-Aldrich) in 20-30 µL of deionised water was incubated on the samples for 30

min (Figure 11 iv)). The samples were then washed with deionised water and dried under a stream of nitrogen followed by the measurement of the optical spectra. After the antibody incubation, albumin chicken egg white (antigen) (from Sigma-Aldrich) in 1 ML of deionised water was incubated for 30 min (Figure 11 v)). The samples were then washed with deionised water and dried under a stream of nitrogen.

4.3.Topographic and optical techniques

An Atomic Force Microscope (AFM) and an optical spectrometer were used to characterize the samples produced in the MaSCA system. The main purpose of the AFM was to get a topographic imaging of the sample to analyse the distribution and the density of clusters on the surface. The AFM Ntegra Aura (from NT-MDT) was used in a semi-contact mode using standard commercial silicon cantilevers with curvature radius of tip better than 10 nm.

To analyze the topographic images collected, the software Image Analysis 2.1.2 (from NT –MDT) was used to determine the height of the deposited clusters. Figure 15 shows an example of an AFM image collected and a cross section of a deposited cluster.

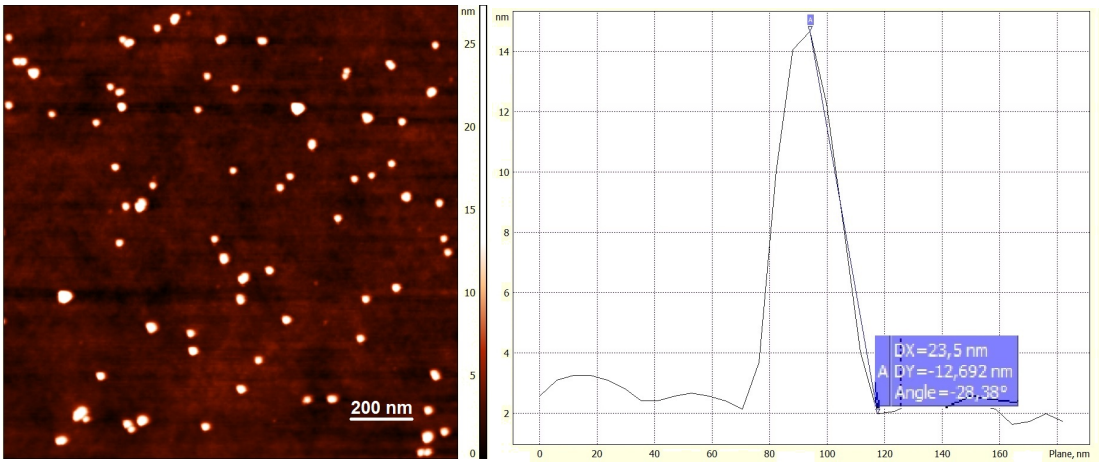

i) ii)

Figure 15 – A topographic AFM image of a sample with size-selected clusters deposited on a thin PMMA film can be seen in i) and the analysis of a cross section of a deposited cluster selected from i) utilizing the software from NT-MDT in ii)

Optical spectroscopy measurements were performed by double beam Perkin Elmer High Performance Lambda 1050 Spectrometer in a standard configuration in the UV-Visible region of the spectrum (300-750 nm). The optical spectra were collected in transmission mode.

The plasmon resonance characterization of the protein deposition first requires the optical characterization of the plasmon resonance of the bare silver nanoparticles deposited in PMMA. To check the quality and sensitivity of the transducers produced, the plasmon peak position and absorbance intensity were measured, which are sensitive to the clusters density, shape and size (Figure 16).

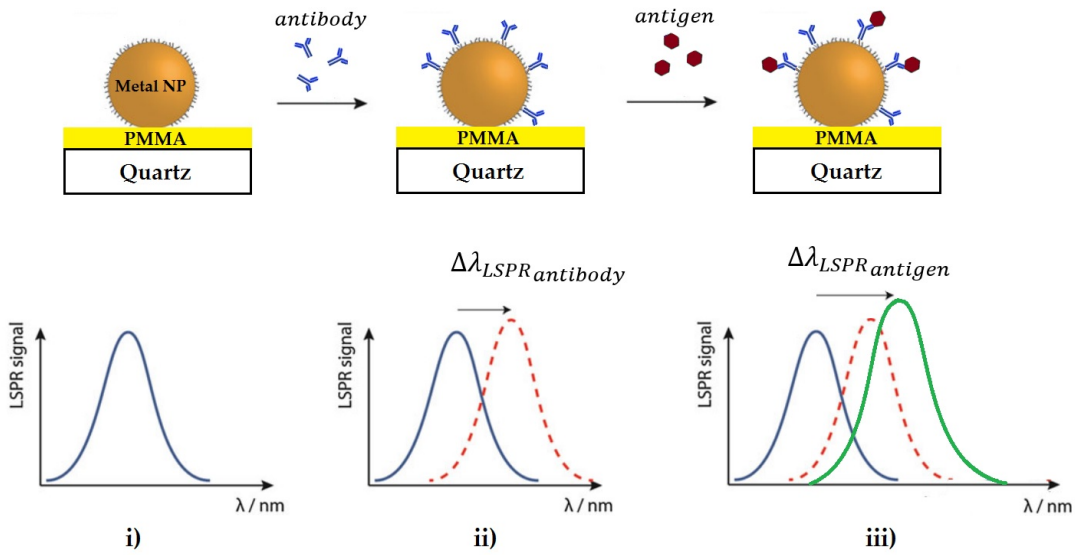

Figure 16 – Schematic representing the three steps of the plasmon sensing. i) plasmon band for size-selected silver clusters deposited on PMMA; ii) plasmon band for the antibodies incubated on silver clusters; iii) plasmon band for the antigens attached to antibodies, adapted from [45].

The plasmon resonance of bare silver clusters (Figure 16 i)) will be the reference for the proteins that will be deposited and the sensing will be measured by the shifts of the λ_{max} observed on the spectra. The plasmon resonance peak position is then obtained by measuring the transmittance of the samples, which fulfils the conditions mentioned above. The measured transmittance spectrum is converted into absorbance using the relation:

$$A = 2 - \log(T\ \%) \tag{4.1}$$

As previously mentioned on the clusters PMMA interaction section, metal clusters are deposited on PMMA with different hardness (*hard*, *soft*, and *viscous*) with the same parameters of production and deposition presented on Table II. The samples will be characterized regarding the size of the clusters and their optical properties, which are dependent on the way the clusters are deposited in PMMA with different types of annealing. In all experiments, a constant voltage of $\pm 300\ V$ was applied to the EQMS.

5. Results and Discussion

The discussion of the results obtained for the size-selected silver clusters deposited on PMMA thin films is divided into the AFM characterization of the topographic images and optical spectroscopy results for the absorption spectra of the samples for protein sensing.

5.1. AFM characterization of nano-biosensors

In this work, topographic AFM measurements were carried out for all the samples produced to first characterize the heights of the size-selected silver clusters deposited on PMMA layers. However, due to the different viscosities of the polymer and the embedment of silver clusters into them, the relative height measured will not be corresponded to the actual clusters size, i.e. the characterization will be focused only in the embedment process in *viscous* and *soft* PMMA layers.

Through AFM measurements, subsequently confirmed with transmission electron microscopy (TEM) measurements [46], it was found that the clusters preserve almost spherical shape after the deposition becoming just slightly oblate [40]. Thus, it is safe to assume that the clusters height measured on AFM topographic images is almost equal to their diameter and the term size is synonym for the height and diameter.

Also, it should be mentioned that specific regions of AFM images were considered for statistical analysis, with the more homogeneous coverage and with less clusters aggregation as possible. In Figure 17, a specific region of an AFM image and corresponding histogram for clusters deposited on *hard* polymer is shown.

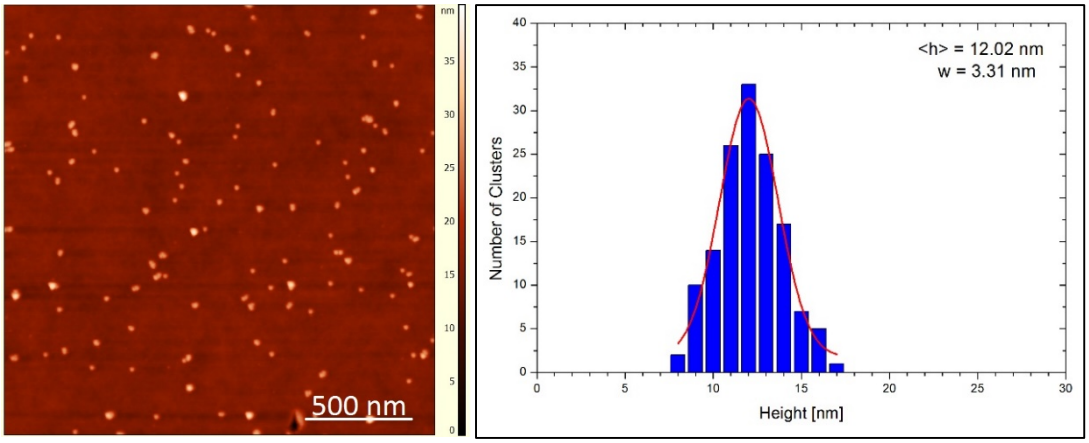

Figure 17 – AFM image and the corresponding height histogram for clusters deposited on a *hard* (***T* = 180**℃) polymer of 100 nm thickness.

From the topographic AFM image, a considerable number of nanoparticles is analysed to have a good statistic of the number of clusters, in order to determine the mean silver clusters height. It should be mentioned that *hard* PMMA means that the polymer was annealed at temperatures above the glass transition, $T = 180$ ℃.

Clusters deposited on *hard* PMMA samples confirm the success of their size-selection through the height histograms (Figure 17), and for this type of PMMA hardness one can say that silver clusters do not embed deeper on polymer layers, staying only at the surface. Table IV lists all the results obtained for *hard* polymers with different thicknesses.

Table IV – Mean values of clusters height deposited on *hard* PMMA of different thicknesses.

Sample Ag/PMMA/Q (**PMMA**: **T = 180** ℃)	**Thickness [nm]**	**Mean Height [nm]**	**Standard Error Height [nm]**	**Standard Deviation [nm]**	**Relative Standard Deviation [%]**	**Number of Clusters**
# 12	35	12.15	0.06 (0.5%)	1.44	12	175
# 09	54	12.02	0.09 (0.7%)	1.65	14	140
# 10	100	12.10	0.09 (0.7%)	3.06	25	134

The mean height, <h>, averaged over 130 clusters on *hard* PMMA of different thicknesses, from the Gaussian function is (12.09 ± 0.07) nm, which is slightly smaller than the mean height for clusters deposited on silicon (12.8 ± 1.5) nm [47], averaged over 500 clusters. One possible reason for this difference might be the low density/counts of clusters on *hard* PMMA samples.

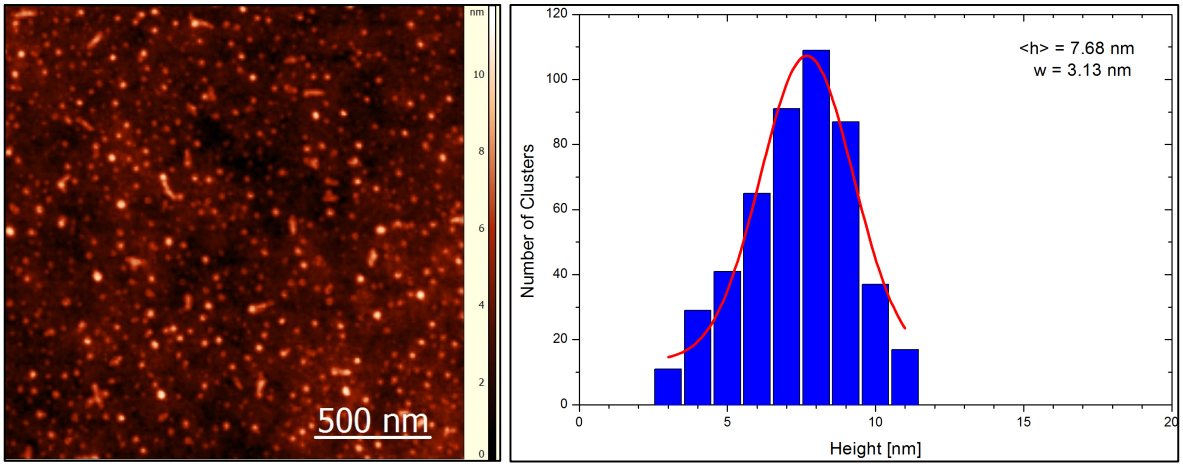

Figure 18 – AFM and the corresponding height histogram for clusters as-deposited on 100 nm *viscous* polymer (sample # 16).

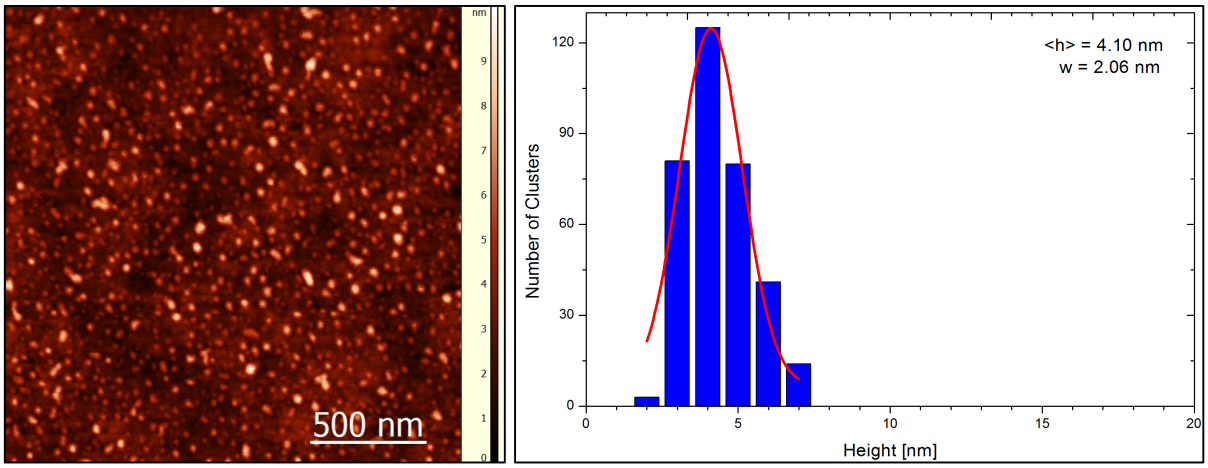

Figure 19 – AFM and the corresponding height histogram for clusters deposited on 100 nm *viscous* polymer, annealed at **95**℃ for 10 min (sample # 16).

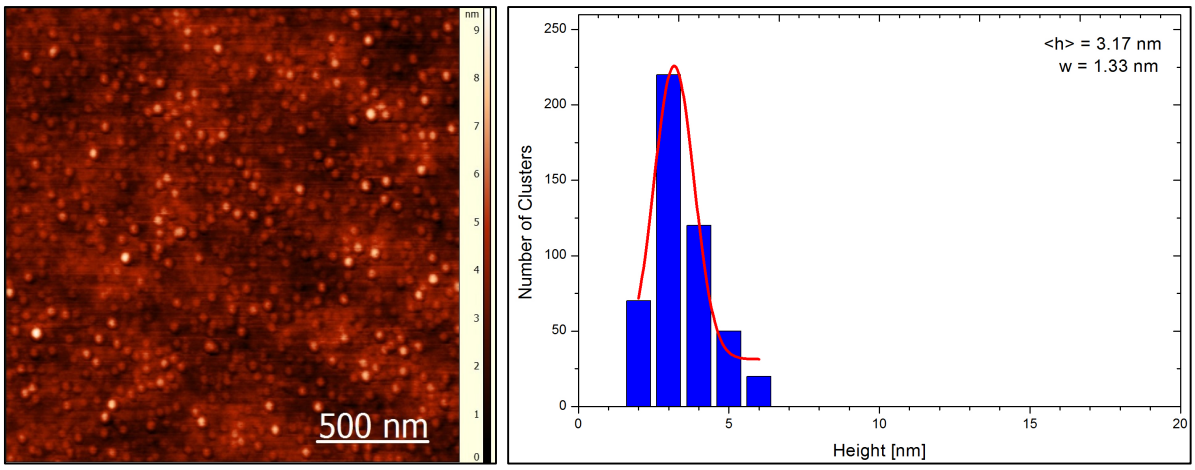

Figure 20 – AFM and the corresponding histogram for clusters deposited on 100 nm *viscous* polymer, annealed at **100**℃ for 10 min (sample # 16).

Regarding the clusters deposited on *viscous* PMMA having different hardnesses, three AFM images, from PMMA with thickness of 100 nm (sample # 16) were analysed (Figure 18, 19, and 20).

Different hardnesses were achieved by heating the PMMA layers at different temperatures after the deposition of clusters (as deposited, 95 ℃ and 100℃), (Table V). Among these three *viscous* PMMA layer, the hardest layer is the one heated at 100 ℃. For the clusters deposited on PMMA 10 nm thick, no AFM images are shown. In this case, it was not possible to get the heights due to the high density of clusters which results in their agglomeration.

AFM images collected for these samples with as-deposited clusters show that the mean height of clusters has decreased to around 8 nm with a wide size distribution and a long tail towards smaller particle heights. It can be suggested that the deposited clusters are partly immerse into the polymer due to its low hardness and high viscosity [46].

Table V – Mean values of clusters height deposited on *viscous* PMMA.

Sample Ag/PMMA/Q	PMMA d[nm]	T [°C]	time [min.]	Mean Height [nm]	Standard Error Height [nm]	Standard Deviation [nm]	Relative Standard Deviation [%]	# Clusters
		RT	---	---	---	---	---	---
# 19	10	95	30	11.83	0.13 (1%)	2.72	23	276
		100	15	13.05	0.06 (0.5%)	2.41	18	403
		RT	---	7.68	---(1%)	3.13	40	490
# 16	100	95	5	4.10	---(0.5%)	2.06	50	390
		100	10	3.17	---(0.2%)	1.33	42	480

The next step was to anneal the samples to investigate the immersion of the silver clusters deposited on the PMMA layer. This was performed in two steps, the first one at 95 °C and the second one at 100 °C, both for 10 min. The corresponding AFM images and histograms are shown in Figures 19 and 20.

It is clear that after the first annealing the cluster surface coverage decreases significantly and the <h> becomes much smaller, <h>= 4.10 nm. This effect occurs in the other *viscous* samples prepared at the same conditions but with different PMMA thicknesses. It was also verified that for thicker samples (100 nm), the embedment occurs deeper than in

thinner samples (10 nm). One possible explanation resides on the large amount of PMMA which is not cured. Therefore, during the annealing, the surface energy at the interface of NPs and PMMA would be the driving force for the immersion under higher temperatures.

The second annealing, at $T = 100℃$, also decreased the surface coverage and height for <h> = 3.17 nm. It seems that PMMA under thermal annealing is forcing the NPs to penetrate deeper into the film becoming fully embedded after some time.

Throughout the successive samples' annealing, it can be verified that the clusters density at the PMMA surface increases and their agglomeration tend to disappear, probably due to the differences between the surface energy of the silver clusters and PMMA [31]. This effect was also observed in the other samples produced with different thicknesses.

Regarding *soft* PMMA samples, a similar process was followed for the samples' annealing, with the difference that, before the deposition of silver clusters, the samples were annealed at a temperature below the glass transition, $T = 95℃$.

An AFM image and corresponding height histogram are presented in Figure 21 for 20 nm thick *soft* PMMA. The clusters height in this case is close to the one expected from the previous experiments, around <h> ≈ 13 nm.

This means that the silver clusters stay on the PMMA surface and do not immerse due to the hardness increased by the annealing of the PMMA. Another feature presented on the AFM image is the high density of NPs in the sample, denoting the different layers of NPs deposited possibly due to the surface roughness of the PMMA. For *soft* PMMA samples, the annealing temperature (below the glass transition temperature) has proven not to be sufficient to initiate the clusters immersion.

For a better understanding of the evolution of the clusters density on the PMMA, the sample was annealed after the cluster deposition in two steps: first at 95 °C for 10 min and then at 100 °C for 10 min. In comparison with the *viscous* polymers, the annealing did not produce any considerable change in the height distribution and in the cluster coverage, indicating that temperatures below the glass transition are not sufficient to initiate the immersion of NPs.

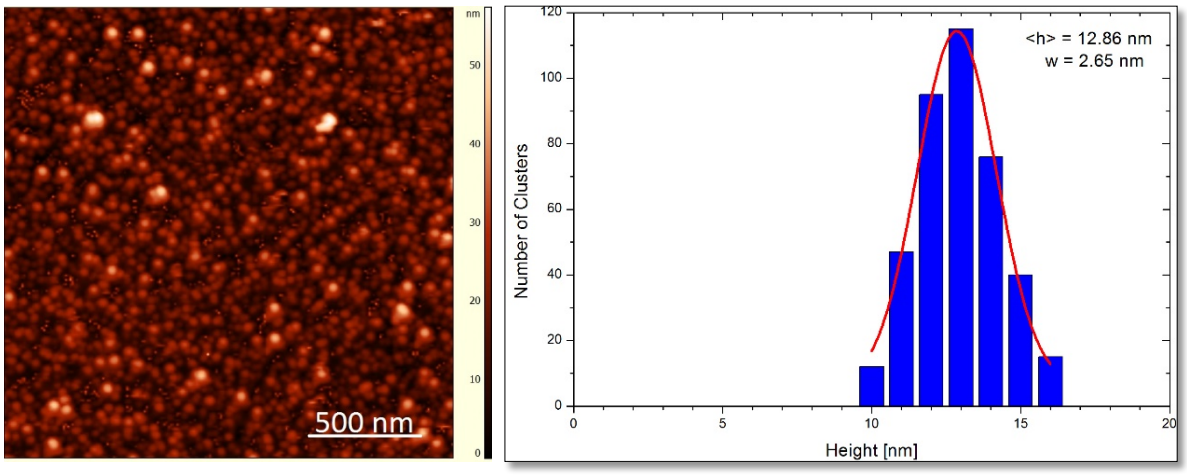

Figure 21 – AFM image and corresponding height histogram for the clusters deposited on *soft* polymer, of 20 nm thickness annealed two times **95**°C; 30 min (sample # 18).

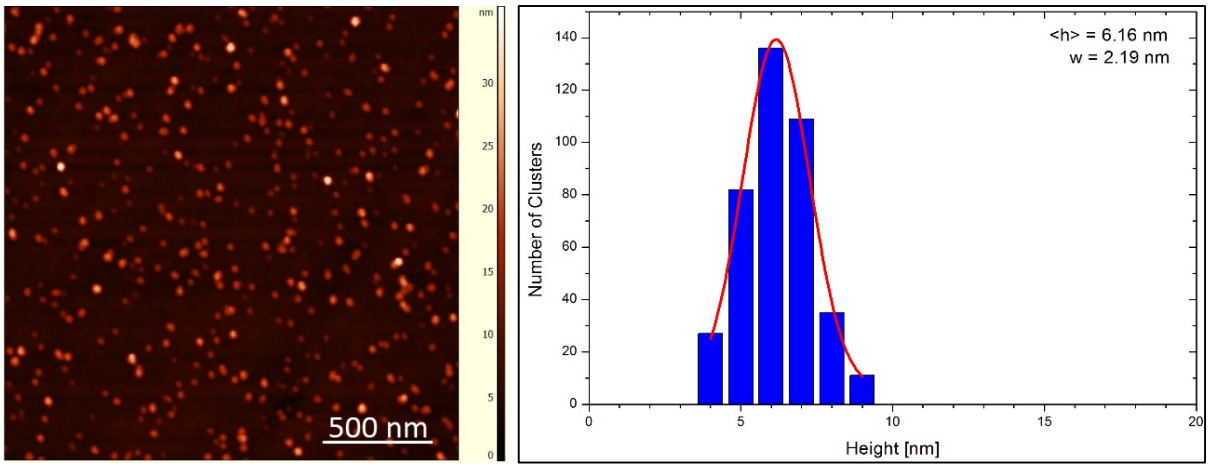

Figure 22 – AFM image and corresponding height histogram for the clusters deposited on *soft* polymer, of 70 nm thickness annealed at **100**°C; 30 min (sample # 18).

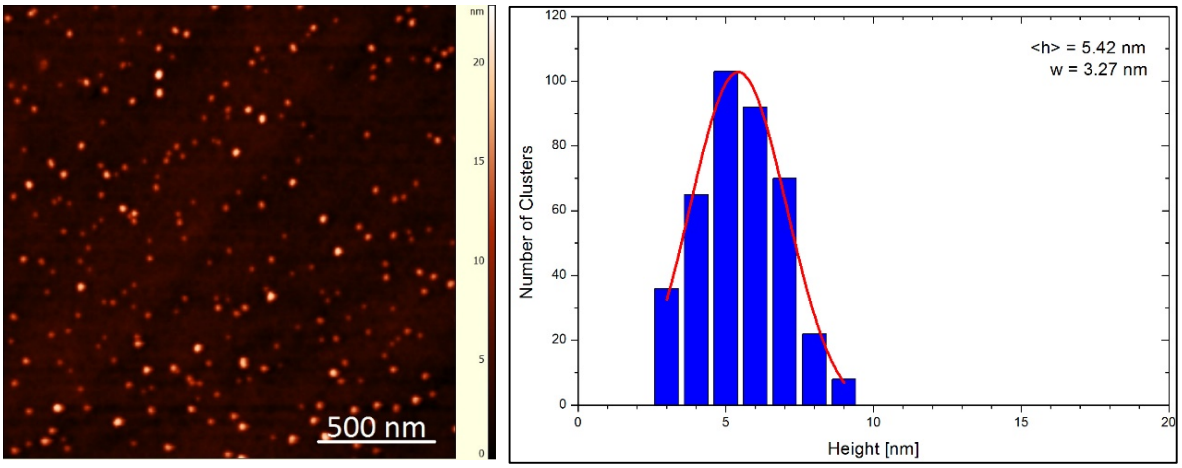

Figure 23 – AFM image and corresponding height histogram for the clusters deposited on *soft* polymer, of 70 nm thickness; annealed at **115**°C; 10 min (sample # 18).

After that, the sample was annealed two times at 100°C and changes of the topography are found to be significant (Figure 22). The nanoparticles height decreases from <h>=12.86 nm to <h>=6.16 nm and the surface coverage becomes much lower, meaning that there was an embedding of Ag NPs into the PMMA.

This means that the difference in surface energy between the silver clusters and the PMMA facilitate the clusters to immerse into the polymer due to its chain mobility. Another annealing was done, this time at $T = 115℃$, and it was found that the nanoparticles height continued to decrease to <h>=5.42 nm. This will reinforce the theory that the immersion of clusters into the PMMA is facilitated by the chain mobility of the polymer.

Table VI shows the mean values of heights of silver cluster for the consequent annealings of the sample 18.

Table VI- Mean values of height, standard errors and standard deviations, and relative standard deviations for the *viscous* PMMA samples.

Sample Ag/PMMA/Q	PMMA d[nm]	T [°C]	time [min.]	Mean Height [nm]	Standard Error Height [nm]	Standard Deviation [nm]
# 18	10	95	---	---	---	---
		100	30	12.86 (1%)	2.65 (9%)	409
		100	30	6.16 (1%)	2.19 (5%)	404
		115	15	5.42 (1%)	3.27 (11%)	397

5.2.Plasmon resonance analysis of nano-biosensors

In order to test the samples as plasmonic transducers, optical measurements were made in the clusters-PMMA nano-composites. From AFM analysis, the most suitable samples with the clusters size-selection and with a high clusters density were chosen to be tested as transducers for nano-biosensors.

Regarding *hard* PMMA samples which were annealed at 180°C before the deposition, the absorption spectrum for the sample with 20 nm PMMA thick did not reveal any plasmon band. In the samples of PMMA with thicknesses of 54 and 100 nm, it was observed two plasmon bands (Figure 24).

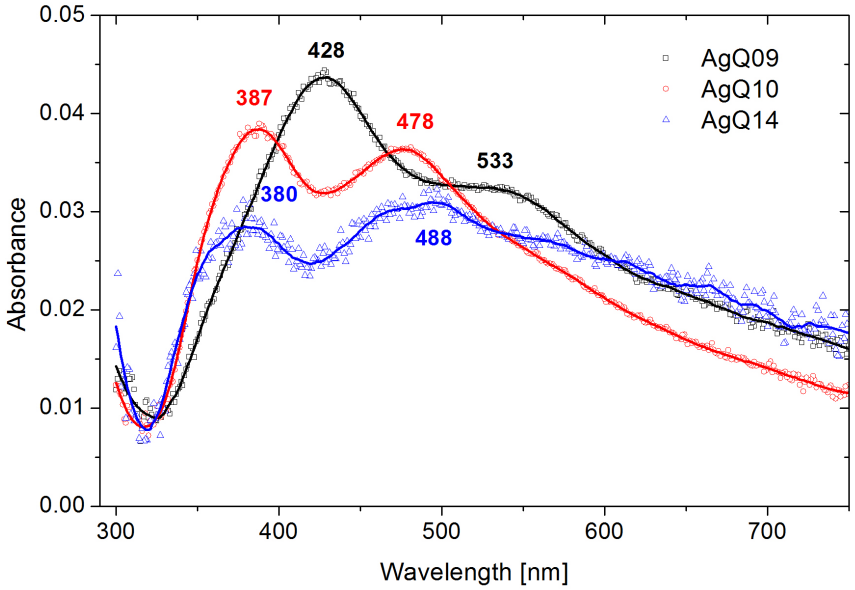

Figure 24 – Normalized absorption spectra for silver clusters deposited on *hard* PMMA with different thicknesses (54 nm PMMA black line, 100 nm PMMA red and blue line).

The overall AFM image for the PMMA sample with 54 nm thickness, from which a specific region was taken for statistical analysis (Figure 17), shows that there are regions with homogeneous deposition of clusters and that the clusters are well separated, but it can also be found regions showing less homogeneous distribution with high concentration of clusters due to their agglomeration. Since the region selected for the absorption measurements will not be exactly the same from those analysed on AFM, the presence of the two plasmon bands can be explained by the agglomeration of silver clusters at the PMMA surface.

A possible explanation for the agglomeration of clusters is the low adherence of the clusters to the PMMA, i.e., the adhesion energy of the clusters is lower than the binding energy between clusters. Clusters have stronger bonds within dimmers than between clusters and PMMA, for regions where the intensity of the cluster beams is higher. From the

experimental point of view, it is expected a higher density of clusters in the centre of the beam, so the aggregation cannot be completely excluded from occurring in that region. Therefore, once deposited, they kept this agglomeration.

Also, these agglomeration effects can lead to a plasmon coupling, which can occur due to the high clusters density on the surface sample, making the distance between clusters smaller so that the phase relations among the scattered light from different clusters will be coherent and this contribution will be observed in the spectra as a form of a second peak [48].

Table VII shows the maximum wavelengths and their intensities for clusters deposited on *hard* polymers with different thicknesses.

Table VII – Wavelength of LSPR maximum (λ_m) and absorbance for spectra in Figure 24.

Sample Ag/PMMA/Q	Thickness [nm]	λ_m [nm]	Absorbance
# **09**	54	428	0.0444
		533	0.0322
# **10**	100	387	0.0383
		478	0.0363
# **14**	100	380	0.0285
		488	0.0308

Regarding *viscous* PMMA, which were annealed after the clusters deposition, the optical absorption for these samples clearly demonstrates an evolution with the samples' annealing. Figure 25 and 26 presents the three steps of the annealing for two samples with different thicknesses, where it is very clear that when the *viscous* samples are annealed at a certain time and temperature, the intensity is increased and the plasmon peak is well defined.

For the first optical absorption spectrum measured after the deposition, for the sample with PMMA thickness of 100 nm (Figure 25, black line, sample #16), there are presented two different peaks at λ_{max}= 384 nm and λ_{max}= 479 nm. As discussed before for *hard* samples, the first peak can be related to the plasmon resonance of silver clusters and the second one to the plasmon-coupling due to the agglomeration of silver clusters. Through AFM images and their histograms, it can be suggested that due to the hardness of the polymer, clusters are immersed in the *viscous* PMMA and some agglomerate due to

viscosity of the PMMA, which allows the formation of dimers that can easily happen during cluster deposition due their self-assembly.

After the sample's annealing at a temperature below the glass transition, $T = 95$ ℃, the first plasmon band is increased three times than the previous one and the band is shifted to higher wavelengths, or as is usually called "red" shift, to a maximum wavelength of $\lambda_{\max}$ = 408 nm (Figure 25, green line).

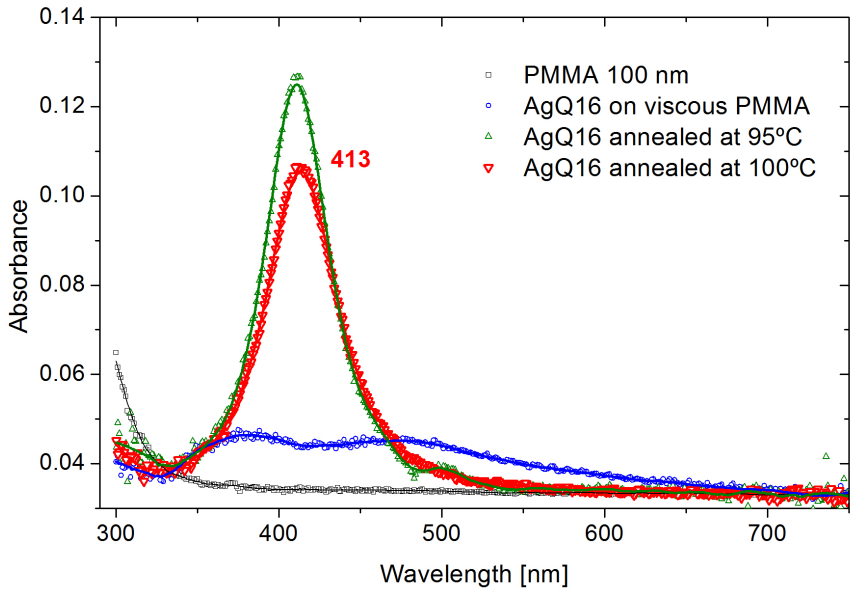

Figure 25 – Normalized optical absorption spectra measured for silver clusters deposited on *viscous* PMMA with 100 nm thickness (blue line), and their evolution with subsequent annealing at **95**℃ (green line) and **100**℃ (red line).

The topographic analysis suggests that the significant changes in the optical proprieties results can be correlated to the embedment of NPs on the PMMA, which decreases the clusters surface coverage and changes the dielectric environment of the silver clusters. The fact that the dielectric constant of PMMA ($\varepsilon_{r\,PMMA} = 2.6$) is higher than the air ($\varepsilon_{r\,air} = 1$), affects directly the optical spectra observed which can be proved by equation (4.2). The samples' annealing allows the clusters to rearrange in the polymer, meaning that the interparticle distances will increase, which results in a diminishing of the second plasmon band, possibly due to the break of self-assembled pairs of clusters formed at the surface of the PMMA during their deposition.

Another annealing was performed in the sample to check if the plasmon peak intensity will continue increasing due to heating (Figure 25, red line). This time, the sample was annealed at 100℃, and the intensity decreased, and although the plasmon band red shifted to $\lambda_{max} = 413$ nm, which is the expected maximum wavelength for the extinction coefficient for the silver clusters of this given size.

A similar procedure was done for the *viscous* sample with a 20 nm thick PMMA (Figure 26), but it was found that after the first annealing, i.e. at $T = 95$℃, the plasmon band to higher wavelengths did not disappear, probably due to the thinner PMMA film which allow the clusters to agglomerate much easier than for thicker PMMA films. A second annealing at the same temperature was done but it was not observed any significant change, most likely due to the hardness of the polymer and the clusters aggregation at the PMMA surface.

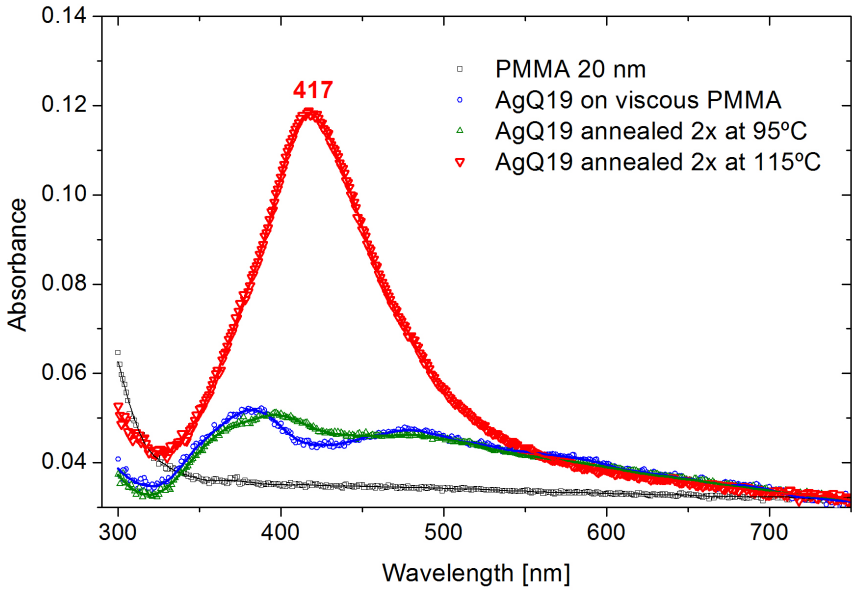

Figure 26 – Normalized optical absorption spectra measured for silver clusters deposited on *viscous* PMMA with 20 nm thickness (blue line), and their evolution with subsequent annealing, two times at **95**℃ (green line) and one at **115**℃ (red line).

After the second annealing, the obvious path for the samples annealing was to increase the annealing temperature to $T = 115$℃, which reveal significant changes to the optical spectrum. The plasmon band increased in its intensity and there was a red shit to $\lambda_{max} = 417$ nm, which is close to the theoretical wavelength for silver clusters ($\lambda_{max} = 413$ nm) with $d = 13$ nm. It was also found that for thinner PMMA films (sample # 19), the temperatures used for the annealing should be higher.

This was verified when PMMA films with 10, 20 and 50 nm thickness were used. With the increasing of PMMA thickness, less annealing processes were necessary and the annealing temperature was lower. This effect can be explained due to the polymer hardness. For thicker samples the viscosity is maintained and the immersion of clusters is provided, whereas for thinner films there is a faster solidification, meaning that higher temperatures are needed to provide the immersion of the clusters into the polymer.

One of the challenges for PMMA with higher thicknesses is related to the process of getting a sharp plasmon resonance peak for the silver clusters embedded deep into the polymer, which is the process of isolation of clusters without many annealings with high temperatures. This test was also carried out with other *viscous* samples, where the same effects were verified, which are presented in the Table VIII.

Table VIII – Wavelength of LSPR maximum ($\boldsymbol{\lambda_m}$) and band intensity for spectra in Figure 25 and 26.

Sample Ag/PMMA/Q	**Thickness [nm]**	**Temperature annealing** [℃]	$\boldsymbol{\lambda_{max}}$ **[nm]**	**Absorbance**
# 19	20	---	384	0.0517
			479	0.0473
		2x 95 (for 5 min)	397	0.0511
			480	0.0464
		115 (for 15 min)	417	0.1182
# 16	100	---	381	0.0467
			472	0.0452
		95 (for 5 min)	411	0.1267
		100 (for 15 min)	413	0.1063

Regarding *soft* PMMA samples, two optical analysis were made for silver clusters deposited on PMMA with thickness of 10 nm and 20 nm (Figure27 and 28 respectively). A similar procedure of the *viscous* samples was done, with the difference that PMMA was annealed at a temperature below the glass transition ($T = 95$℃) before the clusters deposition (blue line of Figure 27 and 28).

After the deposition, the optical spectroscopy measurement for *soft* PMMA with as-deposited clusters show that, like in *viscous* samples, two plasmon bands in the same wavelengths are formed. As discussed in the AFM characterization of this sample, as-deposited silver clusters stay on the PMMA surface and do not immerse (Figure 21), which will provide their aggregation on the polymer surface, resulting in the second plasmon band already discussed. However, after the first two samples' annealing, that were performed at a temperature below the glass transition ($T = 100$℃), the peak corresponding to the plasmon coupling almost disappeared, being only characterized by the plasmon band in the $\lambda_{max} = 418$ nm (Figure 27, green line, representing the second annealing).

The AFM analysis of this sample (Figure 22), that gives the height distribution of silver clusters, it can be said that during the annealing, the surface energy at the interface of NPs and PMMA will force their immersion and the clusters that were agglomerate will break and rearrange on the polymer. It should be noted that for temperatures above the glass transition, the embedment process is verified due to their dependence on the polymer chain mobility.

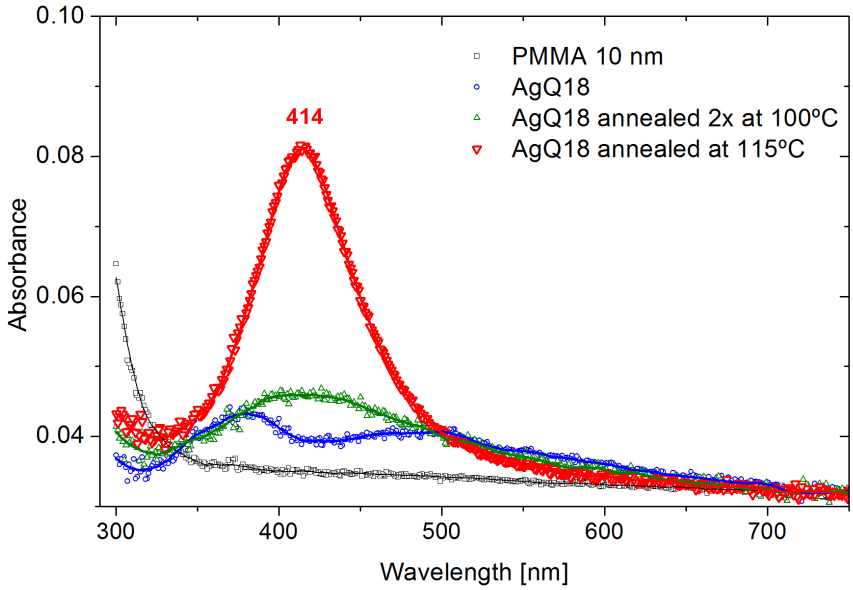

Figure 27 – Normalized optical absorption spectra measured for silver clusters deposited on *soft* PMMA with 10 nm thickness (blue line), and their evolution with subsequent annealing, two times at **100**℃ (green line) and one at **115**℃ (red line).

After annealing at $T = 115$℃, the spectrum has a sharp plasmon band (Figure 27, red line), with an increase of its intensity, and a red shift of the peak is verified to a maximum of $\lambda_{max} = 414$ nm. The second band is almost vanished for the same reason as in the case of *viscous* PMMA.

In the case of sample # 29 (Figure 28), the same results are verified, with the difference that after the first annealing the sample revealed to have a good evolution in the immersion of silver clusters into PMMA, which lead to an increase of the plasmon band intensity. Like sample #18, the vanish of the second band is related to the plasmon coupling.

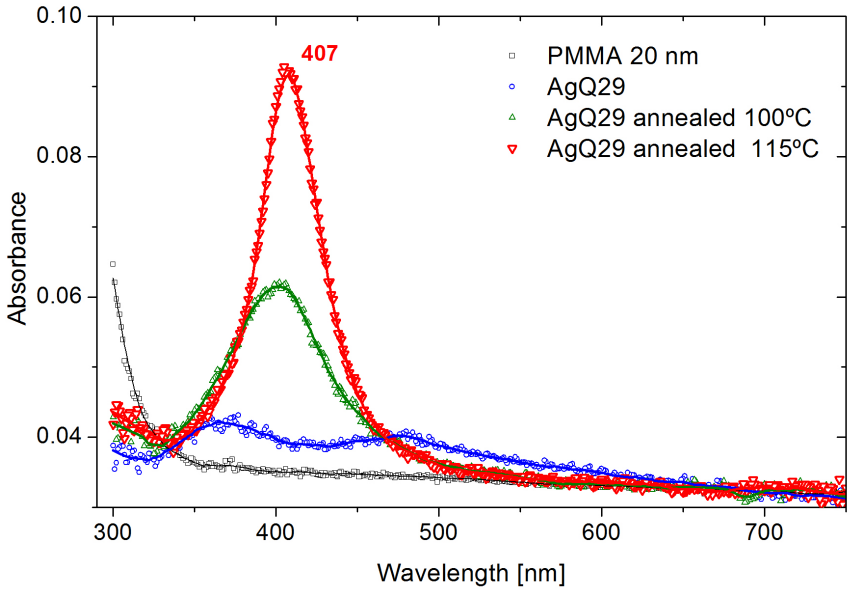

Figure 28 – Normalized optical absorption spectra measured for silver clusters deposited on *soft* PMMA with 100 nm thickness (blue line), and their evolution with subsequent annealing at **100**℃ (red line) and **115**℃ (blue line).

The last annealing of the sample #29, at $T = 115$℃, also revealed a red shift and an increase of the intensity of the plasmon band at $\lambda_{max} = 407$ nm.

In table IX are presented the maximum wavelengths and their absorbance intensities of the soft samples analysed.

Table IX – Wavelength of LSPR maximum λ_m and band intensity for spectra in Figure 26 and 27.

Sample Ag/PMMA/Q	λ_{max} **[nm]**	**Temperature annealing** [℃]	**Absorbance**	**Δ Absorbance**
# 18	20	no annealing	379	0.0432
			483	0.0405
		2x at 100 (for 30 min.)	418	0.0469
		115 (for 15 min.)	414	0.0811
# 29	20	no annealing	369	0.0423
			476	0.0404
		100 (for 30 min.)	402	0.0620
		115 (for 15 min.)	407	0.0923

After the optical measurements, the samples which were likely able to get a good response to LSPR were used as transducers for protein sensing. Samples with clusters embedded in PMMA layers clearly demonstrate the presence of a narrow and intensive LSPR absorption band at 407-417 nm after their thermal annealing, which will be the reference for protein sensing.

As discussed in the previous section of AFM characterization, *hard* PMMA samples lead to the aggregation of clusters in the surface, since they have low adherence to the surface. This will affect the wet chemistry process for protein deposition, resulting in a lowering of the peak intensity of the plasmon band due to the decrease of clusters density at the PMMA surface. Therefore, the study for protein sensing will only be centred on *viscous* (Figure 29 and 30) and *soft* (Figure 31 and 32) polymers which reveal better results in the protein detection.

As mentioned in the experimental methods for the nano-biosensors, the scheme used for detection is centred in an antibody-antigen interaction. The proper analysis of the optical absorption spectra should be focused in the qualitative biosensing through the red shift of the plasmon band to higher wavelengths, and afterwards their quantification. Figure 29 and 30 presents two different absorption spectra for the samples prepared with *viscous* PMMA, with the same parameters in the deposition of silver clusters, but with different PMMA thicknesses. It is clear that the incubation of the antibody on the deposited clusters leads to the shift of the plasmon peak towards higher wavelengths.

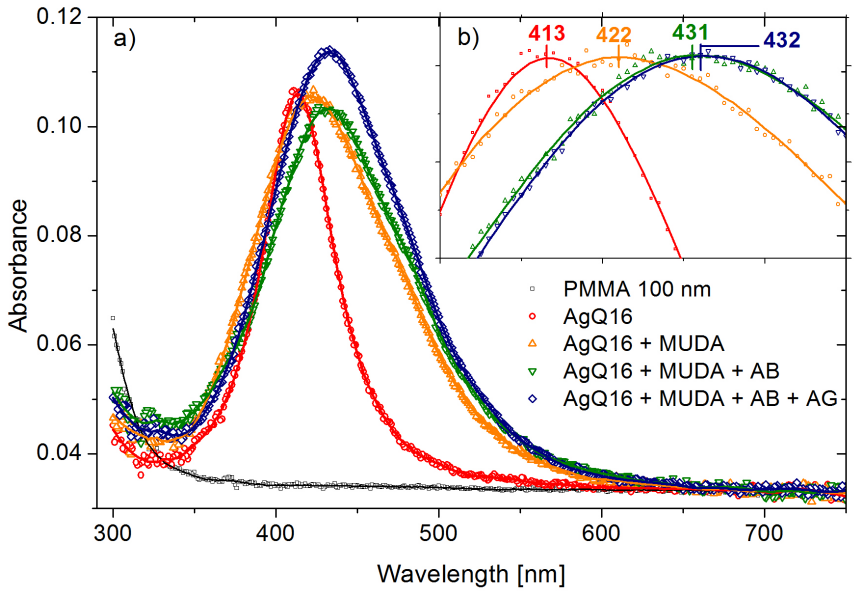

Figure 29 – Normalized optical absorption spectra to the background (a)) and to the maximum concentration (b)), measured for silver clusters deposited on 100 nm *viscous* PMMA, followed by steps for the incubation of proteins.

It should also be noted that the absorption spectra were normalized to the background (Figure 27 a)) and to its maximum (Figure 28 b)). From the normalization to the background, the absorbance intensities can be measured, but for a normalization to its maximum, only the information about the shifts can be used

The optical spectra for the viscous PMMA sample 16 clearly demonstrates the protein detection through the red shifts of the plasmon band. After the functionalization with MUDA (Figure 29, orange line), the plasmon band increased to a maximum wavelength of $\lambda_{max} = 422$ nm, although its full width at half maximum (FWHM) was broader which reveals that probably some clusters that were not well embedded on PMMA were vanished during the wet chemistry, making the intensity of the absorbance lower and the plasmon peak broader. With the antibody-antigen deposition, a significant shift was observed, of $\lambda_{max} = 431$ nm for the antibody and $\lambda_{max} = 432$ nm for the antigen.

Regarding the sample # 19, the same effect happened of the broader FWHM for MUDA can be seen, but this time the red shift of the plasmon band is only $\lambda_{max} = 418$ nm (Figure 30, orange line). With the incubation of antibody and antigen the plasmon bands clearly demonstrate similar values with the ones for the sample # 16 (Figure 30, green and blue line respectively).

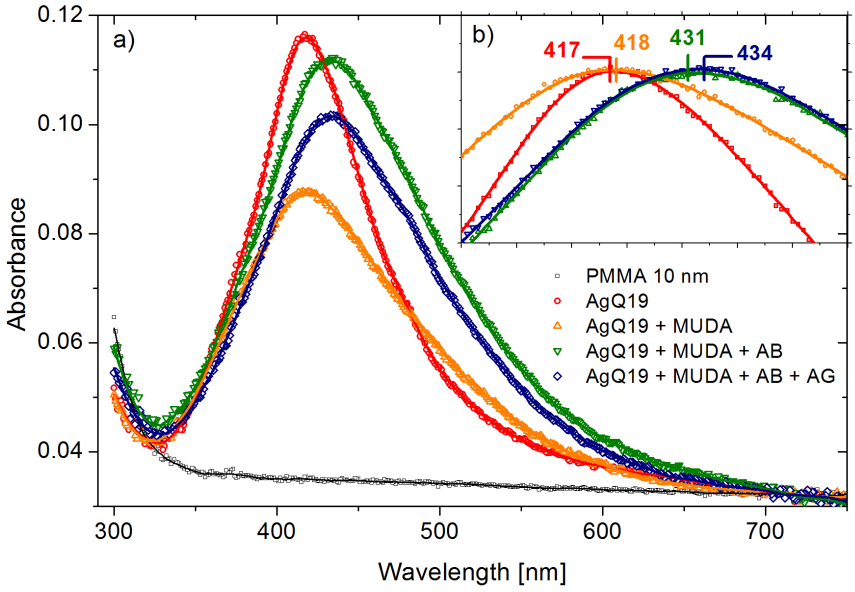

Figure 30 – Normalized optical absorption spectra to the background (a)) and to the maximum concentration (b)), measured for silver clusters deposited on 10 nm *viscous* PMMA, followed by steps for the incubation of proteins.

Table X show the values of the plasmon bands regarding each step of the protein incubation for viscous samples.

Table X – Wavelength of LSPR maximum λ_m and band intensity for spectra in Figure 29 and 30.

Sample Ag/PMMA/Q		λ_{max} [nm]	$\Delta\lambda$ [nm]	Absorbance	Δ Absorbance
# 16	----	413	0	0.1060	0
	MUDA	422	+9	0.1055	-0.0005
	Anti-Body	431	+18	0.1033	-0.0027
	Anti-Gene	432	+19	0.1136	+0.0076
# 19	---	417	0	0.1159	0
	MUDA	418	+1	0.0876	-0.0283
	Anti-Body	431	+14	0.1119	-0.0004
	Anti-Gene	434	+17	0.1015	-0.0144

For *soft* polymers, the features regarding the plasmon shift when the antibody is deposited and after antigen, are similar to those observed for the viscous polymers. Meaning that the red shifts present same amplitude and the also an increasing in intensity.

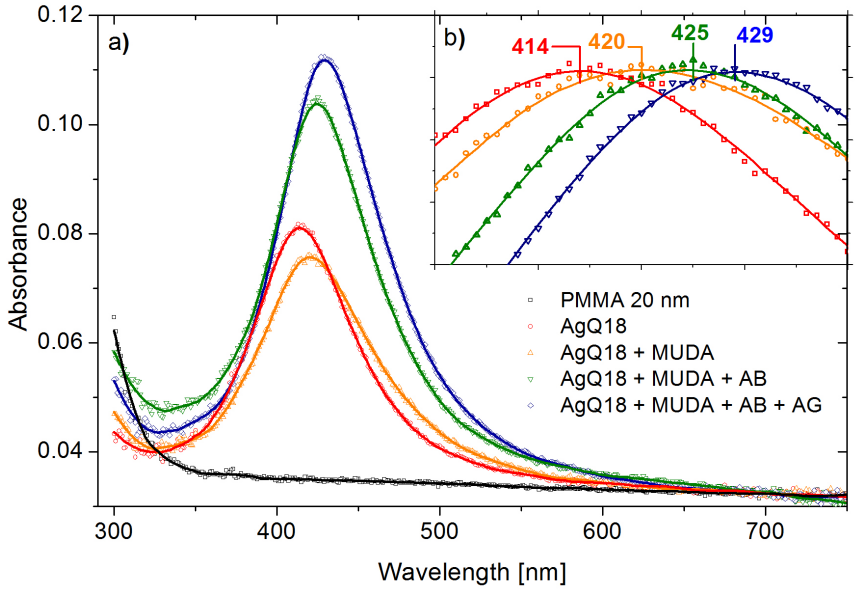

Figure 31 – Normalized optical absorption spectra to the background (a)) and to the maximum concentration (b)), measured for silver clusters deposited on 20 nm *soft* PMMA, followed by steps for the incubation of proteins.

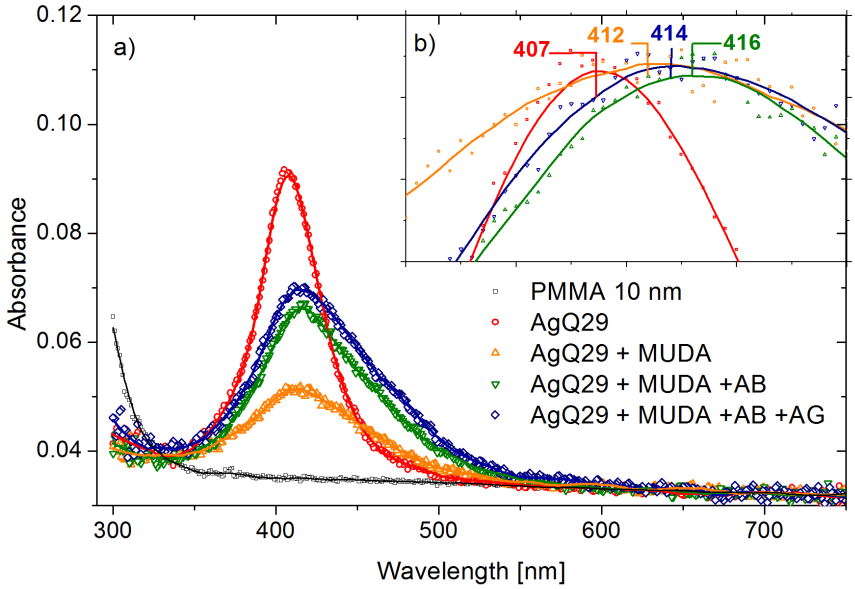

Figure 32 – Normalized optical absorption spectra to the background (a)) and to the maximum concentration (b)), measured for silver clusters deposited on 10 nm *soft* PMMA, followed by steps for the incubation of proteins.

In the case of soft viscous on soft polymer with 10 nm thickness the functionalization of MUDA induces a broader FHWM, suggesting that the ethanol coming from MUDA solution can have an effect in PMMA layer.

Table XI shows the maximum wavelengths for the plasmon bands regarding soft samples.

Table XI – Wavelength of LSPR maximum (λ_m) and band intensity for spectras in Fig. 24.

Sample Ag/PMMA/Q		λ_{max} [nm]	$\Delta\lambda$ [nm]	Absorbance	Δ Absorbance
# 18	---	414	0	0.0810	0
	MUDA	420	+6	0.0757	-0.0053
	Anti-Body	425	+11	0.1037	+0.0227
	Anti-Gene	429	+15	0.1118	+0.0308
# 29	---	407	0	0.0905	0
	MUDA	412	+5	0.0514	-0.0391
	Anti-Body	416	+9	0.0660	-0.0245
	Anti-Gene	414	+7	0.0696	-0.0209

In Figures 33, 34 and 35, can be seen the difference between AFM images of bare silver clusters deposited on PMMA and the AB/AG incubation in the three different types of PMMA hardness, *hard, viscous* and *soft*, respectively. The three AFM topographic images show an increase of the average height size when compared before and after the protein incubation.

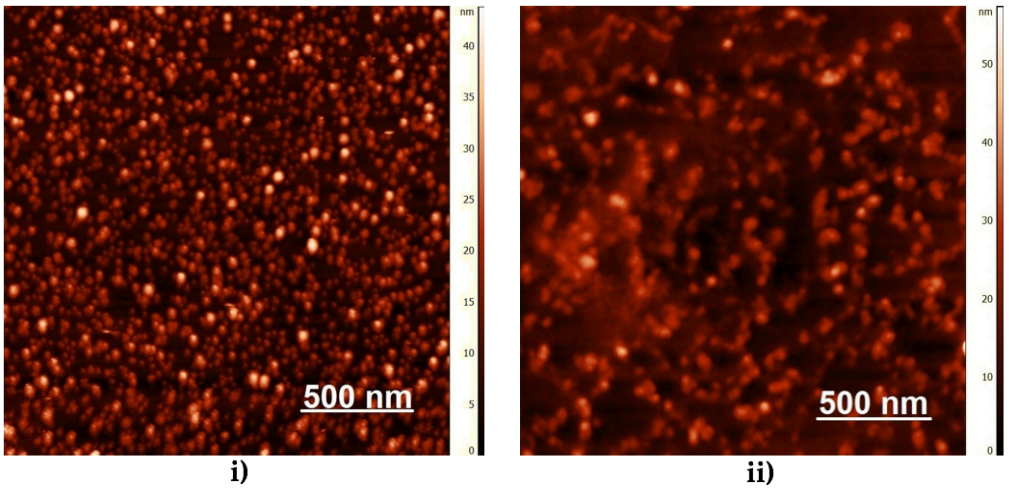

Figure 33 – AFM image of *hard* sample # 9 corresponding to the silver clusters deposited on *hard* PMMA i) and after the antibody incubation in this sample ii).

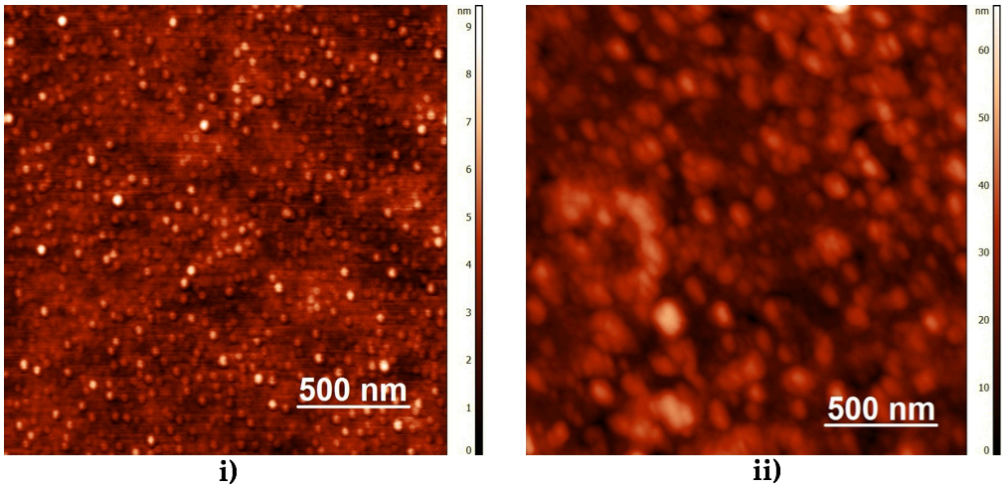

Figure 34 – AFM image of *viscous* sample # 16 corresponding to the silver clusters deposited on *viscous* PMMA i) and after the antigen incubation in this sample ii).

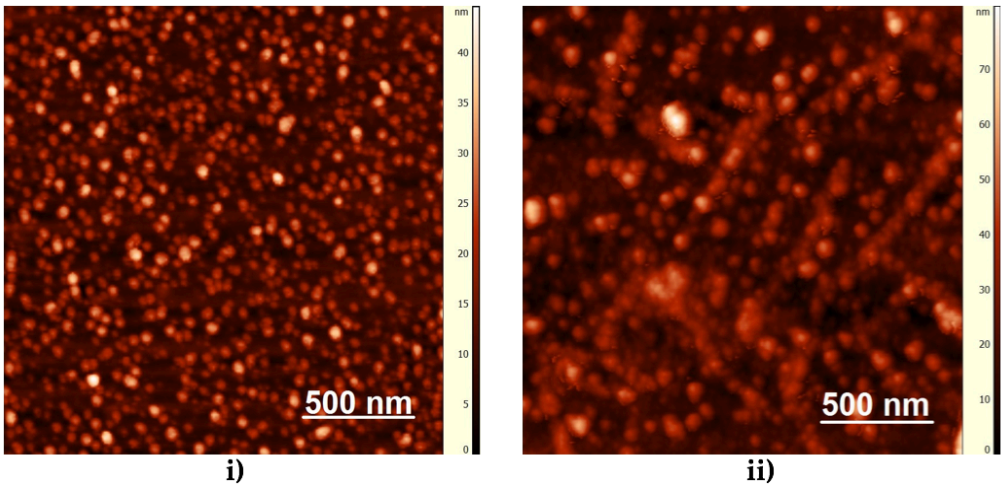

Figure 35 – AFM image of *soft* sample # 18 corresponding to the silver clusters deposited on *soft* PMMA i) and after the antigen incubation in this sample ii).

6 Conclusions and Future Perspectives

The purpose of this project was centered in the production of size-selected silver clusters and their deposition on substrates with PMMA layers with different viscosities, nanomaterials and their application for biosensing. These goals were successfully reached.

After a series of experiments with different types of polymer hardness, the procedure was optimized in three types of metal-polymer composites to develop transducers for biosensing. Through thermal annealing, *hard*, *viscous* and *soft* PMMA layers were spin-coated in quartz substrates giving different regimes of nanoparticles immersion into PMMA. These nanoparticles, which were partly or fully embedded on PMMA, showed remarkable plasmonic properties in comparison with previous methods adopted in nano-biosensing.

The supported silver clusters with plasmonic properties were tested for detection of proteins utilizing the phenomenon of localized surface plasmon resonance. For the formation of optical transducers based on silver clusters deposited on quartz substrates with PMMA thin films, a special protocol was developed to deposit proteins of interest.

These transducers proved to sense biological material with an antibody-antigen scheme through localized surface plasmon resonance, where after the deposition a significant shift in the plasmon peak was observed.

It would be very interesting in the future to be able to study and to test, systematically, the effective capability of this systems as biosensors with other proteins and in different polymers presenting different optical constant but more importantly, with different surface tension and elasticity and their behavior with temperature.

References

[1] Marketsandmarkets.com, "Biosensors Market by Application (POC, Home Diagnostics, Research Labs, Biodefense, Environmental Monitoring, Food & Beverages Industry), Technology, Product (Wearable and Non-Wearable), and Geography - Global Forecast to 2022." [Online]. Available: http://www.marketsandmarkets.com/Market-Reports/biosensors-market-798.html. [Accessed: 15-Apr-2017].

[2] V. K. Khanna, *Nanosensors: Physical, Chemical, and Biological*. CRC Press, 2016.

[3] I. E. Tothill, "Biosensors for cancer markers diagnosis," *Semin. Cell Dev. Biol.*, vol. 20, no. 1, pp. 55–62, 2009.

[4] B. S and B. S, "Plasmonic Sensors for Disease Detection - A Review," *J. Nanomed. Nanotechnol.*, vol. 7, no. 3, p. 1000373, 2016.

[5] W. Zhang, A. M. Asiri, D. Liu, D. Du, and Y. Lin, "Nanomaterial-based biosensors for environmental and biological monitoring of organophosphorus pesticides and nerve agents," *TrAC - Trends Anal. Chem.*, vol. 54, pp. 1–10, 2014.

[6] E. Petryayeva and U. J. Krull, "Localized surface plasmon resonance: Nanostructures, bioassays and biosensing—A review," *Anal. Chim. Acta*, vol. 706, no. 1, pp. 8–24, Nov. 2011.

[7] M. N. Velasco-Garcia, "Optical biosensors for probing at the cellular level: A review of recent progress and future prospects," *Semin. Cell Dev. Biol.*, vol. 20, no. 1, pp. 27–33, Feb. 2009.

[8] A. C. Huet, P. Delahaut, T. Fodey, S. A. Haughey, C. Elliott, and S. Weigel, "Advances in biosensor-based analysis for antimicrobial residues in foods," *TrAC - Trends Anal. Chem.*, vol. 29, no. 11, pp. 1281–1294, 2010.

[9] P. Arora, A. Sindhu, N. Dilbaghi, and A. Chaudhury, "Biosensors as innovative tools for the detection of food borne pathogens," *Biosens. Bioelectron.*, vol. 28, no. 1, pp. 1–12, 2011.

[10] J. M. Irudayaraj, *Biomedical Nanosensors*, 1st ed. Pan Standford, 2012.

[11] L. C. Clark and C. Lyons, "ELECTRODE SYSTEMS FOR CONTINUOUS MONITORING IN CARDIOVASCULAR SURGERY," *Ann. N. Y. Acad. Sci.*, vol. 102, no. 1, pp. 29–45, Dec. 1962.

[12] L. Su, W. Jia, C. Hou, and Y. Lei, "Microbial biosensors: A review," *Biosens. Bioelectron.*, vol. 26, no. 5, pp. 1788–1799, 2011.

[13] M. Li, S. K. Cushing, and N. Wu, "Plasmon-enhanced optical sensors: a review," *Analyst*, vol. 140, no. 2, pp. 386–406, 2015.

[14] A. J. Haes and R. P. Van Duyne, "A Nanoscale Optical Biosensor: Sensitivity and Selectivity of an Approach Based on the Localized Surface Plasmon Resonance Spectroscopy of Triangular Silver Nanoparticles," *J. Am. Chem. Soc.*, vol. 124, no. 35,

pp. 10596–10604, Sep. 2002.

[15] P. D. Howes, R. Chandrawati, and M. M. Stevens, "Colloidal nanoparticles as advanced biological sensors," *Science (80-.).*, vol. 346, no. 6205, pp. 1247390–1247390, Oct. 2014.

[16] K. Wegner, P. Piseri, H. V. Tafreshi, and P. Milani, "Cluster beam deposition: a tool for nanoscale science and technology," *J. Phys. D. Appl. Phys.*, vol. 39, no. 22, pp. R439–R459, 2006.

[17] V. N. Popok, "Energetic cluster ion beams: Modification of surfaces and shallow layers," *Mater. Sci. Eng. R Reports*, vol. 72, no. 7–8, pp. 137–157, 2011.

[18] P. Fojan, M. Hanif, S. Bartling, H. Hartmann, I. Barke, and V. N. Popok, "Supported silver clusters as nanoplasmonic transducers for protein sensing," *Sensors Actuators B Chem.*, vol. 212, pp. 377–381, Jun. 2015.

[19] R. L. Johnston, "Clusters : Types , Sizes and Experiments," in *Atomic and Molecular Clusters Master's Series in Physics and Astronomy*, 1st ed., R. L. Johnston, Ed. CRC Press, 2002, pp. 1–30.

[20] S. Sugano, *Microcluster Physics*, vol. 20. Berlin, Heidelberg: Springer Berlin Heidelberg, 1991.

[21] U. Kreibig and M. Vollmer, *Optical Properties of Metal Clusters*, vol. 25. Berlin, Heidelberg: Springer Berlin Heidelberg, 1995.

[22] C. F. v Weizsäcker, "Zur Theorie der Kernmassen," *Zeitschrift für Phys.*, vol. 96, no. 7–8, pp. 431–458, 1935.

[23] W. D. Myers and W. . Swiatecki, "Average nuclear properties," *Ann. Phys. (N. Y).*, vol. 55, no. 3, pp. 395–505, 1969.

[24] N. Lang and W. Kohn, "Theory of metal surfaces: charge density and surface energy," *Phys. Rev. B*, vol. 1, no. 12, pp. 4555–4568, 1970.

[25] B. M. Smirnov, *Principles of Statistical Physics: Distributions, Structures, Phenomena, Kinetics of Atomic Systems*. Wiley, 2006.

[26] B. Smirnov, *Cluster Processes in Gases and Plasmas*. John Wiley & Sons, Inc., 2009.

[27] H. Hartmann, V. N. Popok, I. Barke, V. Von Oeynhausen, and K.-H. H. Meiwes-Broer, "Design and capabilities of an experimental setup based on magnetron sputtering for formation and deposition of size-selected metal clusters on ultra-clean surfaces," *Rev. Sci. Instrum.*, vol. 83, no. 7, p. 73304, Jul. 2012.

[28] B. M. Smirnov, "Processes involving clusters and small particles in a buffer gas," *Uspekhi Fiz. Nauk*, vol. 181, no. 7, p. 713, 2011.

[29] V. N. Popok, I. Barke, E. E. B. Campbell, and K.-H. Meiwes-Broer, "Cluster–surface interaction: From soft landing to implantation," *Surf. Sci. Rep.*, vol. 66, no. 10, pp. 347–377, Oct. 2011.

[30] G. J. Kovacs and P. S. Vincett, "Subsurface particle monolayer and film formation in softenable substrates: techniques and thermodynamic criteria," *Thin Solid Films*, vol. 111, pp. 65–81, 1984.

[31] F. Ruffino, V. Torrisi, G. Marletta, and M. G. Grimaldi, "Effects of the embedding kinetics on the surface nano-morphology of nano-grained Au and Ag films on PS and PMMA layers annealed above the glass transition temperature," *Appl. Phys. A*, vol. 107, no. 3, pp. 669–683, 2012.

[32] K. A. Willets and R. P. Van Duyne, "Localized Surface Plasmon Resonance Spectroscopy and Sensing," *Annu. Rev. Phys. Chem.*, vol. 58, no. 1, pp. 267–297, May 2007.

[33] "Plasmonics and Nanophotonics." [Online]. Available: https://nanocomposix.eu/pages/plasmonics-and-nanophotonics. [Accessed: 10-

Aug-2016].

[34] A. J. Haes, S. Zou, G. C. Schatz, and R. P. Van Duyne, "Nanoscale Optical Biosensor: Short Range Distance Dependence of the Localized Surface Plasmon Resonance of Noble Metal Nanoparticles," *J. Phys. Chem. B*, vol. 108, no. 22, pp. 6961–6968, Jun. 2004.

[35] L. S. Jung, C. T. Campbell, T. M. Chinowsky, M. N. Mar, and S. S. Yee, "Quantitative Interpretation of the Response of Surface Plasmon Resonance Sensors to Adsorbed Films," *Langmuir*, vol. 14, no. 19, pp. 5636–5648, 1998.

[36] G. Mie, "Beiträge zur Optik trüber Medien, speziell kolloidaler Metallösungen," *Ann. Phys.*, vol. 330, no. 3, pp. 377–445, 1908.

[37] C. F. A. Negre and C. G. Sánchez, "Optical Properties of Metal Nanoclusters from an Atomistic Point of View," in *Metal Clusters and Nanoalloys*, Springer New York, 2013, pp. 105–157.

[38] J. Hammond, N. Bhalla, S. Rafiee, and P. Estrela, "Localized Surface Plasmon Resonance as a Biosensing Platform for Developing Countries," *Biosensors*, vol. 4, no. 2, pp. 172–188, Jun. 2014.

[39] M. Hanif and V. N. Popok, "Magnetron Sputtering Cluster Apparatus for Formation and Deposition of Size-Selected Metal Nanoparticles," *Physics, Chem. Appl. Nanostructures*, no. May, pp. 416–419, 2015.

[40] M. Hanif, R. R. Juluri, M. Chirumamilla, and V. N. Popok, "Poly(methyl methacrylate) composites with size-selected silver nanoparticles fabricated using cluster beam technique," *J. Polym. Sci. Part B Polym. Phys.*, vol. 54, no. 12, pp. 1152–1159, Jun. 2016.

[41] A. Ahmad and E. Moore, "Electrochemical immunosensor modified with self-assembled monolayer of 11-mercaptoundecanoic acid on gold electrodes for detection of benzo[a]pyrene in water," *Analyst*, vol. 137, no. 24, p. 5839, 2012.

[42] J. M. Berg, J. L. Tymoczko, and L. Stryer, *Biochemistry, Fifth Edition*. W.H. Freeman, 2002.

[43] J. M. Berg, J. L. Tymoczko, and L. Stryer, *Biochemistry, Fifth Edition*. W.H. Freeman, 2002.

[44] "Antibodies: An Industry Almost Ready to Attack." [Online]. Available: http://www.pharmaceutical-technology.com/features/feature63997/feature63997-3.html. [Accessed: 21-Apr-2017].

[45] E. Martinsson and D. Aili, "Refractometric Sensing Using Plasmonic Nanoparticles," in *Encyclopedia of Nanotechnology*, Dordrecht: Springer Netherlands, 2015, pp. 1–11.

[46] M. Hanif, R. R. Juluri, P. Fojan, and V. Popok, "Polymer films with size-selected silver nanoparticles as plasmon resonance-based transducers for protein sensing," *Biointerface Res. Appl. Chem.*, vol. 6, no. 5, pp. 1564–1568, 2016.

[47] M. Hanif and V. N. Popok, "Magnetron Sputtering Cluster Apparatus for Formation and Deposition of Size-Selected Metal Nanoparticles," *Physics, Chem. Appl. Nanostructures*, no. May, pp. 416–419, 2015.

[48] T. Atay, J.-H. Song, and A. V Nurmikko, "Strongly Interacting Plasmon Nanoparticle Pairs: From Dipole−Dipole Interaction to Conductively Coupled Regime," *Nano Lett.*, vol. 4, no. 9, pp. 1627–1631, Sep. 2004.